

Learning inelastic constitutive models from stress–strain data under hard thermodynamic constraints

Filippo Masi¹

¹*Univ. Grenoble Alpes, Inria, CNRS, Grenoble INP, Institute of Engineering, LJK, 38000 Grenoble, France.*

Abstract

Machine learning approaches informed by physics have offered new insights into the discovery of constitutive models from data, helping overcome some limitations of traditional constitutive modelling while reducing the cost of otherwise computationally intensive simulations. Yet, most existing approaches only partially enforce the requirements of physics and thermodynamics, leaving open questions about their consistency across a broad range of material behaviours and their ability to generalise robustly to unseen loading paths when only limited measurements are available.

This work establishes a thermodynamics-constrained learning framework whose architecture embeds the principles of non-equilibrium thermodynamics, material objectivity and stability as hard, scalable constraints to learn constitutive models from standard macroscopic data. Analytical benchmarks involving simple stress-strain loading paths demonstrate that the method learns thermodynamically consistent and robust constitutive models for a range of inelastic materials of increasing complexity. At inference, the resulting models generalise to more demanding, unobserved paths and can autonomously recover interpretable internal variables that capture path-dependent evolution. The framework is then applied to granular media, prototypical heterogeneous and history-dependent materials for which constitutive modelling remains challenging. Trained on numerically simulated experiments based on the discrete element method, the model discovers the underlying constitutive equations and predicts responses under cyclic loading, including the emergence of hysteresis absent from the training data, relying solely on macroscopic stress–strain histories. The approach and findings indicate that enforcing non-equilibrium thermodynamics through hard constraints represents a principled route to robust, consistent, and scalable data-driven discovery of constitutive models.

Keywords Machine learning; Data-driven constitutive modelling; Hard-constrained learning; Non-equilibrium thermodynamics; Dissipation inequality; Inelasticity; Granular materials.

1 Introduction

A central objective in solid mechanics and material science is to predict and understand the response of materials to external stimuli. In continuum mechanics, this predictive capability hinges on the constitutive closure, which complements kinematics and balance equations (e.g. momentum balance) and links observable measures of deformation to stresses and to the evolution of the material state. Beyond accuracy, constitutive models must satisfy structural requirements dictated by physics, including frame indifference and consistency with the laws of thermodynamics. Yet, for materials displaying path-dependent behaviours and intrinsic microstructural effects, traditional heuristic constitutive models are often hindered by phenomenological choices of the state variables and the evolution equations, typically refined through iterative, human-guided adjustments. Multiscale modelling overcomes this issue by replacing heuristic idealisations with implicit constitutive closures obtained from direct numerical simulations of nested boundary-value problems posed on representative elementary volumes (auxiliary problems) and the subsequent upscaling of the effective behaviour [28]. However, the high computational cost of these methods – due to repeated, time-consuming solutions of the auxiliary problem – limits their use in real-scale applications.

To address this gap, machine-learning and data-driven methods have been increasingly explored to (i) discover constitutive equations and (ii) build high-fidelity surrogate models directly from available experimental measurements and numerical simulations (for an extensive review, see [26, 60]). A central development is the integration of first principles directly into learning and identification procedures to improve robustness and generalisation while promoting physically consistent predictions (among others, see [3, 15, 24, 25, 33, 39, 42, 43, 45, 49, 50, 54, 57, 69, 71, 86]). A key design choice

is how physical principles are imposed: through soft constraints (penalisation in the loss) or hard constraints (admissibility by construction). Soft constraints are straightforward to integrate into standard architectures and optimisation algorithms [43], but do not guarantee the fulfilment of the physical principles at inference, particularly under extrapolation outside the training distribution. This can lead to “silent” failures, i.e., plausible yet unphysical predictions without an explicit indicator of inconsistency. Hard constraints, in contrast, enforce the prescribed principles exactly during training and at inference by restricting the hypothesis class a priori, which is found to strengthen generalisation capabilities while providing guarantees of consistency. The trade-off is reduced flexibility: hard constraints often require tailored parameterisations and may limit predictive performance if the imposed structure is overly restrictive or does not align with the observed material behaviour. In practice, both formulations have proved valuable, and hybrid strategies are now common for their flexibility.

In elasticity, several successful approaches learn free-energy potentials using objective inputs, (poly-)convex parameterisations, and Sobolev training [17] to predict the material stress from automatic differentiation, which explicitly enforce material objectivity, well-posedness, and energy balance (cf. [10, 45, 49, 50]).

For inelastic and complex materials, an increasing number of methods leverage plasticity-inspired formulations and the internal variable approach to account for the path-dependent and multiscale behaviour of materials (see [3, 7, 8, 15, 25, 26, 34, 54, 57, 69, 71, 81, 82], among others). Here, the second law of thermodynamics [18] plays a central role in identifying admissible evolution equations and has been enforced through both soft [57] and hard [25] constraints. In particular, data-driven methods based on (convex) dissipation (pseudo-)potentials provide a principled route to enforce non-negative dissipation by construction and have shown improved robustness and generalisation within their scope [3, 25, 34, 35, 37, 71]. Closely related variational formulations have also been proposed to learn internal variables and coarse-grained dynamics from microscopic data with thermodynamic structure [69]. In parallel, structure-preserving (metriplectic) neural networks based on the GENERIC formalism [66] have been proposed to enforce the first and second laws through hard constraints within a broader non-equilibrium thermodynamic structure [15, 33].

Despite the aforementioned developments, data-driven approaches informed by physics often remain tied to specific constitutive classes (e.g. dissipation-potential formulations) or only partially enforce the requirements from physics. This can limit their consistency and scalability across a broad range of material behaviours and their ability to generalise robustly to unseen loading paths when only limited measurements are available.

The aim of this work is to retain the key advantages of hard thermodynamic constraints and to develop a general and scalable framework for discovering constitutive models from conventional labelled stress–strain data (Figure 1). Building on thermodynamics-based artificial neural networks [55, 57], objective and convex energy-potential formulations (cf. [45, 49]), and integral formulations of the evolution equations [52], the proposed approach introduces a learning architecture that defines a class of admissible constitutive models by construction. The model is built on a structured, parametric state space s and a set of trainable neural parameters θ through two coupled parameterisations: an energy density $\psi_\theta(s)$ and a state-dependent transport operator $\mathbb{L}_\theta(s)$ governing the evolution of s , as depicted in Figure 1. The second law is enforced exactly by relying on generalised transport equations [30, 79], rooted in non-equilibrium thermodynamics [18]. This formalism generalises Onsager–Casimir reciprocity relations [9, 63, 64] and provides a systematic decomposition of reversible and irreversible contributions to the state evolution, without requiring an underlying dissipation-potential structure. The best-fit parameters θ^* are then obtained by minimising the mismatch between predicted stress and the available measurements, yielding the final data-driven constitutive closure (Figure 1).

The performance and capabilities of the method are assessed on synthetic measurement datasets generated from analytical material models of increasing complexity, including elasto- and hypo-plasticity, rate effects, hardening, and non-associative flow rules. The discovered models are shown to (i) generalise to unobserved loading paths, (ii) automatically recover interpretable internal variables where needed, and (iii) identify consistent thermodynamic quantities (free energy and dissipation rate) even when these are not provided as measurements. Appendix B demonstrates the benefits of the present framework against penalty-based (soft) formulations of the dissipation inequality.

The approach is then demonstrated on dry, cohesionless granular media using *in silico* experiments based on the discrete element method [16, 48], with particular attention to aleatoric uncertainty arising from spatial heterogeneity and epistemic uncertainty due to limited observability of microstructural effects and states. Beyond discovering a reliable constitutive model over the observed loading protocols, the method extrapolates to unseen cyclic loading paths, including the emergence of hysteresis absent from the training data, while remaining microstructure-agnostic.

The paper is structured in a way that aims to unfold the physical origin and rationale behind the data-driven framework in Figure 1, followed by a rigorous assessment of its performances. Section 2 outlines the theoretical foundations of non-equilibrium thermodynamics used in this work. Section 3 presents the proposed data-driven framework, with particular emphasis on how hard constraints are enforced by construction in the neural parameterisations of the free-energy density and the transport operator, including objectivity, stability, energy conservation, and the non-negative dissipation inequality.

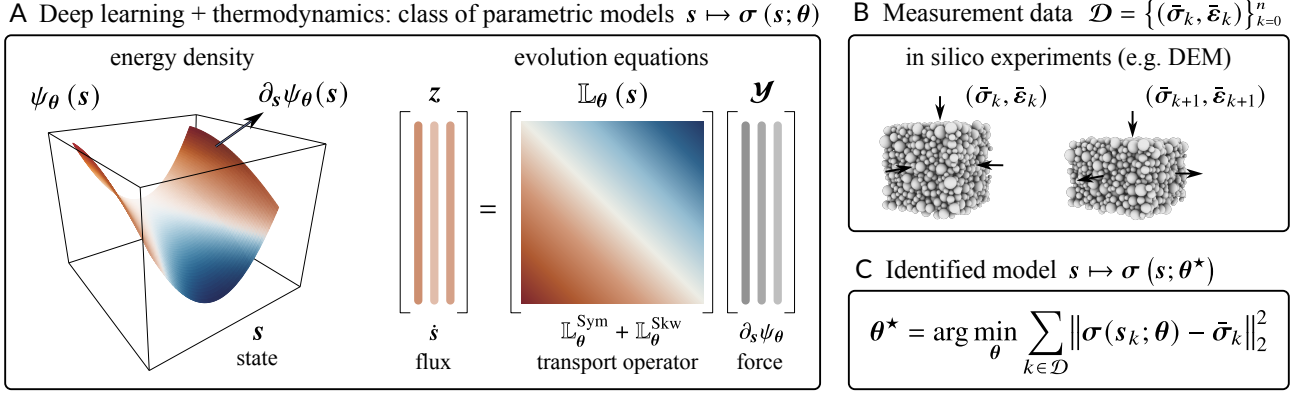


Figure 1: Discovering constitutive models from stress–strain data with hard-constrained non-equilibrium thermodynamics. (A) A thermodynamically admissible constitutive class $s \mapsto \sigma(s; \theta)$, parametrised by the state space s , is built from two neural parametrisations: an energy density $\psi_\theta(s)$, yielding thermodynamic forces $\partial_s \psi_\theta$ (first law), and a transport operator $\mathbb{L}_\theta(s)$ governing the evolution of s while enforcing non-negative dissipation (second law). The networks are defined by a set of trainable parameters θ . The parametric model is trained against (B) discrete-time measurements $\mathcal{D} = \{(\bar{\sigma}_k, \bar{\epsilon}_k)\}$ sampled from in silico experiments as stress-strain pairs to identify (C) a best-fit parametrisation θ^* and the resulting constitutive model $s \mapsto \sigma(s; \theta^*)$.

The resulting class of constitutive equations is then assembled and solved as an initial-value problem at the material element, and the training procedure is detailed. Section 4 assesses accuracy, robustness, and generalisation on analytical material laws. Section 5 studies the application to granular media at the material element level. Finally, Section 6 summarises the main findings and discusses perspectives.

Notation Scalar quantities are denoted by italic symbols (ψ), first-order tensors by bold italic symbols (\mathbf{v}), second-order tensors by lowercase bold symbols ($\boldsymbol{\sigma}$), and higher-order tensors or generalised vectors by uppercase bold symbol (\mathbf{L}, \mathcal{A}). Operator-valued quantities, such as the state-dependent transport operator, are denoted by blackboard bold symbols (\mathbb{L}).

Given arbitrary vectors (\mathbf{a}, \mathbf{b}) and second-order tensors ($\boldsymbol{\sigma}, \dot{\boldsymbol{\epsilon}}$), the inner and outer products are denoted by $\mathbf{a} \cdot \mathbf{b} = a_i b_i$, $\boldsymbol{\sigma} : \dot{\boldsymbol{\epsilon}} = \sigma_{ij} \dot{\epsilon}_{ij}$, and $\mathbf{a} \otimes \mathbf{b} = a_i b_j$, where summation over repeated indices is implied. The generalised inner product between two generalised vectors, \mathbf{A} and \mathbf{B} , collecting quantities of possibly different tensorial order, is denoted by $\mathbf{A} \circ \mathbf{B}$ and is defined component-wise. For example, if $\mathbf{A} \equiv (\mathbf{a} \quad \boldsymbol{\sigma})$ and $\mathbf{B} \equiv (\mathbf{b} \quad \dot{\boldsymbol{\epsilon}})$, then $\mathbf{A} \circ \mathbf{B} \equiv a_i b_i + \sigma_{ij} \dot{\epsilon}_{ij}$.

Spatial gradients of scalar and vector fields and the divergence of vector fields are defined by $(\nabla a)_i = \frac{\partial a}{\partial x_j}$, $(\nabla \mathbf{v})_{ij} = \frac{\partial v_i}{\partial x_j}$, $\text{div } \mathbf{v} = \frac{\partial v_i}{\partial x_i}$. Superposed dots denote material time derivatives, \mathbf{I} is the identity tensor, $\text{tr}(\boldsymbol{\epsilon})$ denotes the trace, and the superscript \top identifies the transpose operation.

2 Non-equilibrium thermodynamics setting

Consider a Cauchy continuum undergoing infinitesimal strains. Thermodynamic processes must comply with (i) the mass balance, (ii) the momentum balance, (iii) the energy balance, (iv) the entropy inequality, and (v) the principles of frame-indifference (objectivity). The point-wise balance of mass, linear momentum, and internal energy read

$$\dot{\rho} + \rho \text{div } \mathbf{v} = 0, \quad (1)$$

$$\rho \dot{\mathbf{v}} - \text{div } \boldsymbol{\sigma} = \rho \mathbf{b}, \quad (2)$$

$$\rho \dot{e} + \text{div } \mathbf{q} = \boldsymbol{\sigma} : \nabla \mathbf{v} + \rho r, \quad (3)$$

Here, ρ is the mass density, e is the specific internal energy (per unit mass), \mathbf{v} is the velocity field, $\boldsymbol{\sigma}$ is the Cauchy stress, \mathbf{b} is the body force density, \mathbf{q} is the heat flux, and r is the specific energy source. The balance of couples is assumed; therefore the stress is symmetric, i.e., $\boldsymbol{\sigma} = \boldsymbol{\sigma}^\top$. The compatibility condition under infinitesimal strain reads $\dot{\boldsymbol{\epsilon}} = \text{Sym}(\nabla \mathbf{v})$.

The entropy balance, or equivalently the second law of thermodynamics, reads [13]

$$\gamma = \rho \dot{s} - \rho T^{-1} r + \text{div } \mathbf{k} \geq 0, \quad (4)$$

where γ is the entropy production, s is the specific entropy, T is the absolute temperature, and \mathbf{k} is entropy flux. In the following, the canonical expression for the entropy flux, i.e., $\mathbf{k} \equiv T^{-1} \mathbf{q}$, is adopted. Note that the entropy flux could be alternatively regarded as a constitutive quantity itself to account for higher-grade materials (see [38, 58, 67, 79]).

Combination of the energy and entropy balance yields the Clausius-Duhem inequality, i.e.,

$$T\gamma = \boldsymbol{\sigma} : \dot{\boldsymbol{\varepsilon}} + \rho [T\dot{s} - \dot{e}] - \frac{1}{T} \mathbf{q} \cdot \nabla T = \boldsymbol{\sigma} : \dot{\boldsymbol{\varepsilon}} - \rho [\dot{\psi} + \dot{T}s] - \frac{1}{T} \mathbf{q} \cdot \nabla T \geq 0, \quad (5)$$

where the last expression is obtained by defining the specific (Helmholtz) free-energy density $\psi \equiv e - Ts$.

In the following, the framework is restricted to isothermal processes ($\mathbf{q} = \mathbf{0}$, $T = \text{const}$) and neglects any covariant derivative (non-local features) to express the thermodynamic constraints in their simplest form. The Clausius-Duhem inequality reduces to

$$d \equiv T\gamma = \boldsymbol{\sigma} : \dot{\boldsymbol{\varepsilon}} - \rho \dot{\psi} \geq 0, \quad (6)$$

where d is the internal dissipation rate.

2.1 Constitutive restrictions and state laws

Following Coleman and Gurtin [13], the state space of a material point \mathbf{x} is described by a set of measurable and controllable state variables, such as the (elastic) strain and an additional set of internal (state) variables that encode the history-dependent state of the material and are non-controllable, i.e., their value cannot be prescribed through boundary conditions [58]. Herein, the state of the material is assumed to be defined by

$$s = (\rho \quad \boldsymbol{\varepsilon}^e \quad \alpha_1 \quad \dots \quad \alpha_{n_\alpha}), \quad (7)$$

where $\boldsymbol{\varepsilon}^e$ is the elastic strain and α_i , with $1 \leq i \leq n_\alpha$, are the n_α internal (state) variables. For compactness of notation, the set of internal variables is denoted as the generalised vector $\boldsymbol{\alpha} \equiv (\alpha_1 \quad \dots \quad \alpha_{n_\alpha})$.

Note that assuming $\boldsymbol{\varepsilon}^e$ as state variable does not imply that the underlying material behaviour is (elasto-)plastic (see Section 4) and it is a modelling choice that improves interpretability and often stabilises optimisation. An alternative is to parameterise the state in terms of the total strain $\boldsymbol{\varepsilon}$, which avoids an explicit decomposition of the strain rate into elastic and irreversible parts, but can make the state representation depend on the (arbitrarily chosen) reference configuration (see [72]). Moreover, in experiments, strains are typically measured incrementally and reported relative to protocol-dependent reference states, thus using $\boldsymbol{\varepsilon}$ can introduce sensitivity to arbitrary offsets across tests. For completeness, Appendix A reports the results obtained with a total-strain parametrisation. Note that the state space may also include higher-order components, e.g., $\nabla \rho$, $\nabla \boldsymbol{\varepsilon}^e$, $\nabla \boldsymbol{\alpha}$ [cf. 67]. Such an extension is fully compatible with the present framework. However, these additional dependencies are omitted to keep the derivation of the transport relations hereafter as simple as possible.

By virtue of the classification of the state space (7), the free energy density is specified as

$$\psi \equiv \psi(\rho, \boldsymbol{\varepsilon}^e, \boldsymbol{\alpha}). \quad (8)$$

To promote material stability, the free energy is required to be convex in the elastic strain (or selected invariants thereof) and the mass density which implies a stable elastic and volumetric response [cf. 4, 74].

The thermodynamic forces conjugate to the state and internal variables are defined as

$$\mu \equiv \rho \frac{\partial \psi}{\partial \rho}(\rho, \boldsymbol{\varepsilon}^e, \boldsymbol{\alpha}), \quad \boldsymbol{\sigma}^e \equiv \rho \frac{\partial \psi}{\partial \boldsymbol{\varepsilon}^e}(\rho, \boldsymbol{\varepsilon}^e, \boldsymbol{\alpha}), \quad \mathcal{A}^e \equiv \rho \frac{\partial \psi}{\partial \boldsymbol{\alpha}}(\rho, \boldsymbol{\varepsilon}^e, \boldsymbol{\alpha}) \quad (9)$$

with μ the chemical potential, $\boldsymbol{\sigma}^e$ the energetic stress, and \mathcal{A}^e the energetic forces associated with the internal variables. Assuming the free energy to be differentiable with respect to the state variables, the time derivative of free energy reads

$$\rho \dot{\psi} = \boldsymbol{\sigma}^e : \dot{\boldsymbol{\varepsilon}}^e + \mu \dot{\rho} + \mathcal{A}^e \circ \dot{\boldsymbol{\alpha}} = \boldsymbol{\sigma}^e : [\dot{\boldsymbol{\varepsilon}} - \dot{\boldsymbol{\varepsilon}}^P] - \rho \mu \text{tr}(\dot{\boldsymbol{\varepsilon}}) + \mathcal{A}^e \circ \dot{\boldsymbol{\alpha}}, \quad (10)$$

where the last expression is obtained by defining the plastic strain rate $\dot{\boldsymbol{\varepsilon}}^P \equiv \dot{\boldsymbol{\varepsilon}} - \dot{\boldsymbol{\varepsilon}}^e$ and specifying the mass balance, i.e., $\dot{\rho} = -\rho \text{tr}(\dot{\boldsymbol{\varepsilon}})$.

Substitution of the time derivative (10) in the Clausius-Duhem inequality (6) yields

$$d = \boldsymbol{\sigma}^e : \dot{\boldsymbol{\varepsilon}}^P + \dot{\boldsymbol{\varepsilon}} : [\boldsymbol{\sigma} - \boldsymbol{\sigma}^e + \rho \mu \mathbf{I}] - \mathcal{A}^e \circ \dot{\boldsymbol{\alpha}} = \boldsymbol{\sigma}^e : \dot{\boldsymbol{\varepsilon}}^P + \boldsymbol{\sigma}^d : \dot{\boldsymbol{\varepsilon}} + \mathcal{A}^d \circ \dot{\boldsymbol{\alpha}} \geq 0, \quad (11)$$

where the dissipative stress $\boldsymbol{\sigma}^d$ and the dissipative driving forces \mathcal{A}^d are defined as

$$\boldsymbol{\sigma}^d \equiv \boldsymbol{\sigma} - [\boldsymbol{\sigma}^e(\rho, \boldsymbol{\varepsilon}^e, \boldsymbol{\alpha}) - \rho \mu(\rho, \boldsymbol{\varepsilon}^e, \boldsymbol{\alpha}) \mathbf{I}], \quad \mathcal{A}^d \equiv -\mathcal{A}^e(\rho, \boldsymbol{\varepsilon}^e, \boldsymbol{\alpha}). \quad (12)$$

The dissipation inequality can thus be recast in the compact bilinear form

$$d = \mathcal{Y} \circ \mathbf{z} \geq 0, \quad \mathcal{Y} \equiv (\boldsymbol{\sigma}^e \quad \mathcal{A}^d \quad \boldsymbol{\sigma}^d), \quad \mathbf{z} \equiv (\dot{\boldsymbol{\varepsilon}}^P \quad \dot{\boldsymbol{\alpha}} \quad \dot{\boldsymbol{\varepsilon}}), \quad (13)$$

where \mathcal{Y} and \mathbf{z} denote the generalised forces and generalised fluxes, respectively.

The next step consists of finding admissible fluxes and forces, i.e., the plastic strain rate $\dot{\boldsymbol{\varepsilon}}^P$, the rate of the internal variables $\dot{\boldsymbol{\alpha}}$, and the dissipative stress $\boldsymbol{\sigma}^d$, that comply with the above dissipation inequality.

2.2 Transport equations

A broad class of solutions of the dissipation inequality (13) is provided by the generalised transport equations [30, 79]

$$\mathbf{z} = \mathbb{L}\mathcal{Y} \quad \text{i.e.} \quad \begin{pmatrix} \dot{\boldsymbol{\varepsilon}}^p \\ \dot{\boldsymbol{\alpha}} \\ \dot{\boldsymbol{\varepsilon}} \end{pmatrix} = \begin{pmatrix} \mathbf{L}^{11} & \mathbf{L}^{12} & \mathbf{L}^{13} \\ \mathbf{L}^{21} & \mathbf{L}^{22} & \mathbf{L}^{23} \\ \mathbf{L}^{31} & \mathbf{L}^{32} & \mathbf{L}^{33} \end{pmatrix} \begin{pmatrix} \boldsymbol{\sigma}^e \\ \mathcal{A}^d \\ \boldsymbol{\sigma}^d \end{pmatrix} \quad (14)$$

where the blocks \mathbf{L}^{ij} of the transport operator \mathbb{L} are in general nonlinear operators mapping the j -th force component to the i -th flux component, and may depend on the state variables and the conjugate forces, $\mathbf{L}^{ij} = \mathbf{L}^{ij}(\mathcal{Y}(s), s)$, along with additional variables, when required.

By decomposing the transport operator into symmetric and skew-symmetric parts, $\text{Sym}(\mathbb{L})$ and $\text{Skw}(\mathbb{L})$, defined with respect to the generalised inner product \circ , the evolution equations read

$$\begin{aligned} \mathbf{z} &= \text{Sym}(\mathbb{L})\mathcal{Y} + \text{Skw}(\mathbb{L})\mathcal{Y} \\ \begin{pmatrix} \dot{\boldsymbol{\varepsilon}}^p \\ \dot{\boldsymbol{\alpha}} \\ \dot{\boldsymbol{\varepsilon}} \end{pmatrix} &= \underbrace{\frac{1}{2} \begin{pmatrix} 2\mathbf{L}^{11} & \mathbf{L}^{12} + \mathbf{L}^{21} & \mathbf{L}^{13} + \mathbf{L}^{31} \\ \mathbf{L}^{21} + \mathbf{L}^{12} & 2\mathbf{L}^{22} & \mathbf{L}^{23} + \mathbf{L}^{32} \\ \mathbf{L}^{31} + \mathbf{L}^{13} & \mathbf{L}^{32} + \mathbf{L}^{23} & 2\mathbf{L}^{33} \end{pmatrix}}_{\text{Sym}(\mathbb{L})} \begin{pmatrix} \boldsymbol{\sigma}^e \\ \mathcal{A}^d \\ \boldsymbol{\sigma}^d \end{pmatrix} + \underbrace{\frac{1}{2} \begin{pmatrix} \mathbf{0} & \mathbf{L}^{12} - \mathbf{L}^{21} & \mathbf{L}^{13} - \mathbf{L}^{31} \\ \mathbf{L}^{21} - \mathbf{L}^{12} & \mathbf{0} & \mathbf{L}^{23} - \mathbf{L}^{32} \\ \mathbf{L}^{31} - \mathbf{L}^{13} & \mathbf{L}^{32} - \mathbf{L}^{23} & \mathbf{0} \end{pmatrix}}_{\text{Skw}(\mathbb{L})} \begin{pmatrix} \boldsymbol{\sigma}^e \\ \mathcal{A}^d \\ \boldsymbol{\sigma}^d \end{pmatrix} \end{aligned} \quad (15)$$

The dissipation inequality thus becomes

$$d = \mathcal{Y} \circ \mathbf{z} = \mathcal{Y} \circ (\text{Sym}(\mathbb{L})\mathcal{Y}) + \mathcal{Y} \circ (\text{Skw}(\mathbb{L})\mathcal{Y}) = \mathcal{Y} \circ (\text{Sym}(\mathbb{L})\mathcal{Y}), \quad (16)$$

because skew-symmetry implies $\mathcal{Y} \circ (\text{Skw}(\mathbb{L})\mathcal{Y}) = 0$ for all \mathcal{Y} . This yields a general decomposition of the evolution equations into dissipative and non-dissipative contributions: the skew-symmetric part provides a purely non-dissipative (often termed gyroscopic, [79]) contribution to the evolution, whereas the symmetric part is solely responsible for dissipation production.

Finally, the dissipation inequality $d \geq 0$ holds for all generalised forces and the corresponding fluxes satisfying the transport form (14) if and only if

$$\mathcal{Y} \circ (\text{Sym}(\mathbb{L})\mathcal{Y}) \geq 0 \quad \text{for all } \mathcal{Y}, \quad (17)$$

which is equivalent to the symmetric part of the transport operator being positive semidefinite, $\text{Sym}(\mathbb{L}) \succeq 0$.

A similar result follows from a classification of the state space based on total strain $\boldsymbol{\varepsilon}$, see Appendix A.

Note that the present framework is intrinsically linked with the extension of non-equilibrium thermodynamics with dual internal variables, proposed by Ván et al. [79]. Although non-local terms (e.g., $\nabla\boldsymbol{\alpha}$) are omitted here, the set $(\alpha_1, \dots, \alpha_{n_\alpha})$ is not fixed a priori and may include dual internal variables. The dual-variables approach unifies the thermodynamic role of (dissipative) internal variables with internal degrees of freedom that possess their own balance equations, enabling the inclusion of micro-inertia effects [6] and the tracking of internal dynamics [5, 79], without the more stringent requirements assumed in the GENERIC framework [66], e.g., the degeneracy conditions.

2.2.1 Dissipation potentials and the standard materials theory

An alternative path to identify thermodynamically admissible fluxes consists of resorting to dissipation rate potentials [61, 62, 85] and the theory of Generalised Standard Materials (GSM [31, 59]). By postulating the existence of a thermodynamic potential $\phi(\mathcal{Y})$, convex and lower semi-continuous, such that the fluxes \mathbf{z} associated with the forces \mathcal{Y} are the gradients of ϕ , i.e., $\mathbf{z} \equiv \partial\phi/\partial\mathcal{Y}$, with the requirement that $\partial\phi(\mathbf{0})/\partial\mathcal{Y} = \mathbf{0}$, the fulfilment of the dissipation inequality is ensured by construction, i.e., $d = \mathcal{Y} \circ \partial\phi/\partial\mathcal{Y} \geq 0$. The same formalism has been extended to constitutive classes not covered by classical GSM (e.g., non-associative plasticity) by introducing implicit representations of (bi-)potentials, cf. the implicit standard materials framework [19, 20]. Despite the many successful applications to inelastic and complex material responses [36, 59], dissipation-potential approaches rely on the a priori existence of such a potential and therefore impose stronger structural requirements than those adopted here. In particular, under sufficient smoothness of the force–flux map $\mathcal{Y} \mapsto \mathbf{z}$, the existence of a dissipation potential requires the Jacobian to be symmetric, i.e., $\partial\mathbf{z}/\partial\mathcal{Y} = (\partial\mathbf{z}/\partial\mathcal{Y})^\top$, together with a symmetric and positive-semidefinite transport tensor \mathbb{L} (for more details, see [79]). Moreover, a dissipation potential can only generate the dissipative part of the evolution equations, whereas the present framework also accommodates non-dissipative (skew-symmetric) contributions.

2.2.2 Onsager–Casimir reciprocity relations

Under the assumption of time-reversal symmetry of the evolution equations, the generalised transport coefficients in Eq. (14) must satisfy the Onsager–Casimir reciprocity relations, i.e., $\mathbf{L}^{21} = \mathbf{L}^{12}$, $\mathbf{L}^{31} = -\mathbf{L}^{13}$, $\mathbf{L}^{32} = -\mathbf{L}^{23}$, where the sign depends on the parity of the associated force–flux pairs under time reversal [9, 18, 63, 64]. These relations were derived in statistical physics from the principle of microscopic reversibility and have since been successfully adopted in the constitutive modelling of inelastic, complex continua (among others, see [22, 23, 40, 41, 53, 84]). However, when the state space includes arbitrary internal variables whose microscopic counterparts and time-reversal parities are unknown, imposing reciprocity may be too restrictive and not always appropriate. This is particularly true when there is no a-priori phenomenological model establishing the physical nature of each state variable. On that basis, the present framework does not enforce the Onsager-Casimir reciprocity relations, by construction. Nevertheless, whenever the internal variables are measurable, their parities are established, and can be connected with microscopic phenomena, reciprocity constraints can be added without otherwise modifying the approach.

For simplicity, the dissipative stress is neglected henceforth, as it is commonly assumed in solid mechanics. The transport equations reduce to

$$\mathbf{z} = \mathbb{L}\mathcal{Y}, \quad \mathcal{Y} \equiv (\boldsymbol{\sigma}^e \quad \mathcal{A}^d), \quad \mathbf{z} \equiv (\dot{\boldsymbol{\epsilon}}^p \quad \dot{\boldsymbol{\alpha}}), \quad \text{i.e.} \quad \begin{pmatrix} \dot{\boldsymbol{\epsilon}}^p \\ \dot{\boldsymbol{\alpha}} \end{pmatrix} = \begin{pmatrix} \mathbf{L}^{11} & \mathbf{L}^{12} \\ \mathbf{L}^{21} & \mathbf{L}^{22} \end{pmatrix} \begin{pmatrix} \boldsymbol{\sigma}^e \\ \mathcal{A}^d \end{pmatrix}. \quad (18)$$

Dissipative stresses can be reintroduced directly via the general form (14), where required.

3 Thermodynamics-constrained constitutive learning

Building on the above non-equilibrium thermodynamic setting, the goal is to identify the free-energy density ψ and the transport operator \mathbb{L} so that the resulting constitutive equations fulfil the thermodynamic principles by construction, irrespective of the range of available measurements. To this end, two general neural network ansätze are parametrised with respect to the set of neural network parameters $\boldsymbol{\theta}$ for the two unknown operators, namely

$$\psi_{\boldsymbol{\theta}}(s) = \psi(s), \quad \mathbb{L}_{\boldsymbol{\theta}}(\mathcal{Y}(s), s) = \mathbb{L}(\mathcal{Y}(s), s), \quad (19)$$

where s denotes the state space and \mathcal{Y} the generalised forces.

3.1 Hard constraints

As detailed in Section 2, the ansätze in (19) are required to satisfy: (i) the state laws (12); (ii) the positive semidefiniteness of the symmetric part of the transport operator; and (iii) the objectivity principle. In addition, the following postulates are additionally considered: (iv) (poly-)convexity of the free energy with respect to the elastic strain and mass density; and (v) vanishing energy and conjugate forces at an equilibrium stress-free configuration. Item (iv) is a sufficient condition for the existence and stability of solutions to boundary-value problems [4, 14], while item (v) ensures the existence of a reference configuration s_{ref} – undeformed ($\boldsymbol{\epsilon}_{\text{ref}}^e = \mathbf{0}$), at finite density $\rho_{\text{ref}} > 0$ and internal state $\boldsymbol{\alpha}_{\text{ref}} = \mathbf{0}$ – which is stress-free and has zero stored energy. Depending on the application, convexity with respect to internal variables $\boldsymbol{\alpha}$ may also be considered (e.g. [25]). In the following, individual internal variables α_i , $1 \leq i \leq n_{\boldsymbol{\alpha}}$, are assumed scalar.

Frame indifference is enforced by using objective arguments. The present framework assumes an isotropic response and therefore parametrises the free energy using isotropic invariants of $\boldsymbol{\epsilon}^e$. An analogous construction is adopted for the transport operator \mathbb{L} , which is parameterised using objective parametrisations of (\mathcal{Y}, s) . Extensions to anisotropy and to non-coaxial stress–strain relations can be obtained by augmenting the state with structural tensors and by adopting equivariant architectures (cf. [32]).

3.1.1 Free-energy parametrisation

Convexity of the free energy with respect to ρ and (invariants of) $\boldsymbol{\epsilon}^e$ is enforced using a partially input-convex neural network [2], which guarantees convexity in the selected inputs through non-negative weights and convex, non-decreasing activations along the convex branch. The resulting energy is convex in the constrained inputs, whereas macroscopic nonlinearities and history effects remain governed by internal-variable dynamics and the transport equations.

Vanishing energy and forces at the reference state s_{ref} are enforced by affine correction terms, namely

$$\psi_{\boldsymbol{\theta}}(s) \equiv \psi_{\boldsymbol{\theta}}^C(s) - \psi_{\boldsymbol{\theta}}^C(s_{\text{ref}}) - \frac{\partial \psi_{\boldsymbol{\theta}}^C}{\partial s}(s_{\text{ref}}) \circ (s - s_{\text{ref}}) \quad (20)$$

where $\psi_\theta^C(s)$ is a partially input convex neural network fed with the invariant representations of the elastic strain, the density, and the internal variables. The reference density ρ_{ref} is treated as trainable network parameter (constrained to be positive), so that the network can identify the stress-free state directly from data. This definition gives, by construction,

$$\psi_\theta(s_{\text{ref}}) = 0, \quad \frac{\partial \psi_\theta}{\partial \rho}(s_{\text{ref}}) = 0, \quad \frac{\partial \psi_\theta}{\partial \boldsymbol{\varepsilon}^e}(s_{\text{ref}}) = \mathbf{0}, \quad \frac{\partial \psi_\theta}{\partial \boldsymbol{\alpha}}(s_{\text{ref}}) = \mathbf{0}, \quad (21)$$

and ensures thermodynamic stability in the invariant representation of $\boldsymbol{\varepsilon}^e$ and ρ .

The thermodynamic forces μ , $\boldsymbol{\sigma}^e$, and \mathcal{A}^e are directly computed by automatic differentiation of the network with respect to its inputs following the definitions in Eq. (9), namely

$$\mu = \rho \frac{\partial \psi_\theta}{\partial \rho}(s), \quad \boldsymbol{\sigma}^e = \rho \frac{\partial \psi_\theta}{\partial \boldsymbol{\varepsilon}^e}(s), \quad \mathcal{A}^e = \rho \frac{\partial \psi_\theta}{\partial \boldsymbol{\alpha}}(s), \quad (22)$$

resulting in the fulfilment of the energy balance by construction, see [57]. Finally, the Cauchy stress $\boldsymbol{\sigma}$ and dissipative driving force \mathcal{A}^d follow from Eq. (12).

3.1.2 Transport-operator parametrisation

To enforce the dissipation inequality, the (unknown) transport operator is split into symmetric and skew-symmetric parts and parametrised as

$$\mathbb{L}_\theta = \mathbb{L}_\theta^{\text{Sym}} + \mathbb{L}_\theta^{\text{Skw}}, \quad \mathbb{L}_\theta^{\text{Sym}} = \mathbb{T}_\theta \mathbb{T}_\theta^\top \succeq 0, \quad \mathbb{L}_\theta^{\text{Skw}} = \begin{pmatrix} \mathbf{0} & \boldsymbol{\ell}_\theta^{21} \\ -\boldsymbol{\ell}_\theta^{21} & \mathbf{0} \end{pmatrix}, \quad \text{with} \quad \mathbb{T}_\theta = \begin{pmatrix} \boldsymbol{\ell}_\theta^{11} & \mathbf{0} \\ \boldsymbol{\ell}_\theta^{12} & \boldsymbol{\ell}_\theta^{22} \end{pmatrix}, \quad (23)$$

where all sub-blocks $\boldsymbol{\ell}_\theta^{ij}$ are the outputs of a feed-forward neural network, i.e., $\boldsymbol{\ell}_\theta^{ij} = \boldsymbol{f}_\theta(\boldsymbol{\mathcal{Y}}(s), s)$. Since $\mathbb{L}_\theta^{\text{Sym}}$ is expressed in terms of its Cholesky factorisation from the lower triangular matrix \mathbb{T}_θ , it is positive semidefinite by construction and Eq. (23) can approximate transport operators while enforcing non-negative dissipation by construction.

The final form of the transport equations reads

$$\begin{pmatrix} \dot{\boldsymbol{\varepsilon}}^p \\ \dot{\boldsymbol{\alpha}} \end{pmatrix} = \begin{pmatrix} \mathbf{L}_\theta^{11} & \mathbf{L}_\theta^{12} \\ \mathbf{L}_\theta^{21} & \mathbf{L}_\theta^{22} \end{pmatrix} \begin{pmatrix} \boldsymbol{\sigma}^e \\ \mathcal{A}^d \end{pmatrix} \quad (24)$$

with

$$\mathbf{L}_\theta^{11} = \boldsymbol{\ell}_\theta^{11} : (\boldsymbol{\ell}_\theta^{11})^\top, \quad \mathbf{L}_\theta^{12} = \boldsymbol{\ell}_\theta^{11} : (\boldsymbol{\ell}_\theta^{12})^\top + \boldsymbol{\ell}_\theta^{21}, \quad (25)$$

$$\mathbf{L}_\theta^{21} = \boldsymbol{\ell}_\theta^{12} : (\boldsymbol{\ell}_\theta^{11})^\top - \boldsymbol{\ell}_\theta^{21}, \quad \mathbf{L}_\theta^{22} = \boldsymbol{\ell}_\theta^{12} : (\boldsymbol{\ell}_\theta^{12})^\top + \boldsymbol{\ell}_\theta^{22} \circ (\boldsymbol{\ell}_\theta^{22})^\top. \quad (26)$$

Note that the skew component does not contribute to entropy production and increases expressiveness by capturing reversible (gyroscopic) couplings between state variables. This enriches the class of admissible evolution laws beyond dissipation-potential-based templates, while preserving thermodynamic admissibility by construction.

3.2 Constitutive update and time integration

The constitutive response under a given loading protocol is obtained by solving the following differential–algebraic system of equations, which couples the evolution equations with the state laws for the stress $\boldsymbol{\sigma}$ and the generalised forces $\boldsymbol{\mathcal{Y}}$,

$$\begin{cases} \dot{\rho} = -\rho \operatorname{tr}(\dot{\boldsymbol{\varepsilon}}) \\ \dot{\boldsymbol{\varepsilon}}^e = \dot{\boldsymbol{\varepsilon}} - \rho \left[\mathbf{L}_\theta^{11} : \frac{\partial \psi_\theta}{\partial \boldsymbol{\varepsilon}^e}(s) - \mathbf{L}_\theta^{12} \circ \frac{\partial \psi_\theta}{\partial \boldsymbol{\alpha}}(s) \right] \\ \dot{\boldsymbol{\alpha}} = \rho \left[\mathbf{L}_\theta^{21} : \frac{\partial \psi_\theta}{\partial \boldsymbol{\varepsilon}^e}(s) - \mathbf{L}_\theta^{22} \circ \frac{\partial \psi_\theta}{\partial \boldsymbol{\alpha}}(s) \right] \\ \boldsymbol{\sigma} = \rho \left[\frac{\partial \psi_\theta}{\partial \boldsymbol{\varepsilon}^e}(s) - \rho \mathbf{I} \frac{\partial \psi_\theta}{\partial \rho}(s) \right] \\ \boldsymbol{\mathcal{Y}} = \left(\rho \frac{\partial \psi_\theta}{\partial \boldsymbol{\varepsilon}^e}(s) \quad -\rho \frac{\partial \psi_\theta}{\partial \boldsymbol{\alpha}}(s) \right) \end{cases} \quad (27)$$

where \mathbf{L}_θ^{ij} are the blocks of the transport operator defined in Eq. (24), for compactness their dependence on \mathbf{s} and \mathcal{Y} is left implicit. The expressions for $\boldsymbol{\sigma}$ and \mathcal{Y} follow directly from the free energy, cf. Eq. (9)–(12).

In the remainder of this section, a displacement-driven setting with prescribed $\boldsymbol{\varepsilon}(t)$ or, equivalently $\dot{\boldsymbol{\varepsilon}}(t)$, is considered for simplicity. When a protocol requires full force control or mixed control, the unknown strain-rate components are recovered by augmenting Eq. (27) with the corresponding algebraic stress constraints (e.g., $\boldsymbol{\sigma} = \text{const}$) and solving the resulting nonlinear system by means of (quasi-)Newton iterations.

3.2.1 Time integration and solution

The initial-value problem for the state and internal variables reads

$$\mathbf{s}(t) = \mathbf{s}_0 + \int_{t_0}^t \dot{\mathbf{s}}(\mathbf{s}(t), \dot{\boldsymbol{\varepsilon}}(t); \boldsymbol{\theta}) dt, \quad \mathbf{s}_0 = (\rho_0 \quad \boldsymbol{\varepsilon}_0^e \quad \boldsymbol{\alpha}_0), \quad \dot{\mathbf{s}} = (\dot{\rho} \quad \dot{\boldsymbol{\varepsilon}}^e \quad \dot{\boldsymbol{\alpha}}) \quad (28)$$

where \mathbf{s}_0 are the initial conditions and $\dot{\mathbf{s}}$ collects the rates of the state and the internal variables given by the right-hand sides of Eq. (27), parametrised with respect to the network parameters $\boldsymbol{\theta}$ and where the dependence on the generalised forces is left implicit through $\mathcal{Y} = \mathcal{Y}(\mathbf{s})$.

The solution of Eq. (28) can be obtained using standard numerical integrators for ordinary differential equations, including explicit and implicit schemes (fixed-step or adaptive). Since the right-hand side $\dot{\mathbf{s}}(\cdot; \boldsymbol{\theta})$ is differentiable and parameterised by neural networks, Eq. (28) can be interpreted as a neural differential equation [11, 52].

In what follows, a generic one-step update is denoted by

$$\mathbf{s}_{n+1} = \Phi_h(\mathbf{s}_n, t_n; \boldsymbol{\theta}), \quad (29)$$

where $\mathbf{s}_n = \mathbf{s}(t_n)$ and $\mathbf{s}_{n+1} = \mathbf{s}(t_{n+1})$ are the discrete-time values of the material state at time t_n and $t_{n+1} = t_n + h$, with h the time step and Φ_h is the integrator. When full force control or mixed control is imposed, the associated algebraic stress constraints are enforced by solving the corresponding nonlinear residual equations using (quasi-)Newton methods.

Once the time-history of the material state \mathbf{s}_n is computed, the evolution of the stress is directly obtained from the state laws, i.e.,

$$\boldsymbol{\sigma}_n \equiv \boldsymbol{\sigma}(\mathbf{s}_n; \boldsymbol{\theta}) = \rho_n \left(\frac{\partial \psi_\theta}{\partial \boldsymbol{\varepsilon}^e}(\mathbf{s}_n) - \rho_n \frac{\partial \psi_\theta}{\partial \rho}(\mathbf{s}_n) \mathbf{I} \right). \quad (30)$$

3.3 Learning constitutive equations from data

Building on the solution of the constitutive equations parameterised by ψ_θ and \mathbb{L}_θ that are hard-constrained to satisfy the principles of non-equilibrium thermodynamics, the aim is to identify the network parameters $\boldsymbol{\theta}^*$ that best fit measured responses under prescribed loading protocols. Measurements may originate from high-fidelity numerical simulations or laboratory experiments. In general, the free-energy density (ψ), the internal variables ($\boldsymbol{\alpha}$), the elastic strain ($\boldsymbol{\varepsilon}^e$) and their rates are not directly accessible, nor can they be inferred a priori without positing a specific constitutive model. The same holds for the thermodynamic conjugate variables ($\boldsymbol{\sigma}^e$, μ , and \mathcal{A}^e). Additionally, in practice, laboratory measurements are often recorded at sparse and irregular time intervals, which render non-trivial the use of incremental formulations (for more details, see [52]).

The appeal of the proposed approach is that, despite the above challenges, it can discover physically consistent internal variables and learn thermodynamically consistent constitutive equations (state laws and evolution equations) in presence of sparse and incomplete measurements. In this work, attention is restricted to the common setting in which only labelled strain–stress pairs and the material density are available, see Figure 1.

3.3.1 Initial conditions

To predict the time evolution of the state variables, initial conditions for the material state are required. While the initial density can be easily known or measured, the elastic strain and the internal variables are not directly accessible unless restrictive assumptions are made (e.g., a fixed energy form).

Following [52] and with the aim of developing a scalable approach able to deal with the broadest range of initial conditions, the initial elastic strain is obtained from the measured initial stress $\bar{\boldsymbol{\sigma}}_0$ and the measured initial density $\bar{\rho}_0$ by solving the nonlinear algebraic equation

$$\mathcal{R}(\mathbf{s}_0, \bar{\boldsymbol{\sigma}}_0; \boldsymbol{\theta}) = \boldsymbol{\sigma}(\mathbf{s}_0; \boldsymbol{\theta}) - \bar{\boldsymbol{\sigma}}_0 = \bar{\rho}_0 \left(\frac{\partial \psi_\theta}{\partial \boldsymbol{\varepsilon}^e}(\mathbf{s}_0) - \bar{\rho}_0 \frac{\partial \psi_\theta}{\partial \rho}(\mathbf{s}_0) \mathbf{I} \right) - \bar{\boldsymbol{\sigma}}_0 = \mathbf{0}, \quad \mathbf{s}_0 = (\bar{\rho}_0 \quad \boldsymbol{\varepsilon}_0^e \quad \boldsymbol{\alpha}_0). \quad (31)$$

Internal variables are initialised to zero, $\alpha_0 = \mathbf{0}$, which does not restrict generality since their definition is non-unique in absence of a specified free-energy function (e.g. [25, 52]). When microstructural descriptors are available, physically motivated initial values (or learned mappings) can be used instead, e.g., via the multiscale approach in [54]. To solve the root-finding problem (31), ε_0^e is treated as an auxiliary learning parameter, which, initialised at zero, is updated by back-propagating the residual $\mathcal{R}(s_0; \theta)$. This strategy yields smoother optimisation dynamics of the training process and lower computing cost with respect to directly finding the root (at every epoch of the training process).

3.3.2 Training

The training process considers a collection of measurement data obtained from different loading protocols indexed by $p = 1, \dots, n_p$. For each protocol p , strain-stress pairs $\{\bar{\sigma}_k^{(p)}, \bar{\varepsilon}_k^{(p)}\}$ and the initial density $\bar{\rho}_0^{(p)}$ are recorded at the discrete physical instants $k = 0, \dots, n_T^{(p)}$, where for notational simplicity $n_T^{(p)} \equiv n_T$ is the number of time samples. The set of measurement data is concisely denoted by

$$\mathcal{D} = \left\{ \bar{\sigma}_k^{(p)}, \bar{\varepsilon}_k^{(p)}, \bar{\rho}_0^{(p)} \right\}_{k=0, \dots, n_T}^{p=1, \dots, n_p}.$$

Training consists of identifying the best-fit network parameters θ^* and the initial value of the elastic strain that minimise the error in the stress predictions and the residual for the initial conditions, namely

$$\theta^* = \arg \min_{\theta} \left[\frac{1}{n_p n_T} \sum_{p=1}^{n_p} \sum_{k=1}^{n_T} \left\| \sigma(s_k^{(p)}; \theta) - \bar{\sigma}_k^{(p)} \right\|_2^2 + \frac{1}{n_p} \sum_{p=1}^{n_p} \left\| \mathcal{R}(s_0^{(p)}, \bar{\sigma}_0^{(p)}; \theta) \right\|_2^2 \right], \quad (32)$$

where $\|\cdot\|_2$ denotes the Euclidean norm applied to stresses in Voigt notation. The stress predictions are given by Eq. (30), i.e.,

$$\sigma(s_k^{(p)}; \theta) = \rho_k^{(p)} \left(\frac{\partial \psi_{\theta}}{\partial \varepsilon^e}(s_k^{(p)}) - \rho_k^{(p)} \frac{\partial \psi_{\theta}}{\partial \rho}(s_k^{(p)}) \mathbf{I} \right). \quad (33)$$

and they rely on the solution of the initial value problem (28) to obtain the material state $s_k^{(p)}$. For each protocol p , the chosen differential-equation integrator produces a discrete trajectory $\{s_n\}_{n=0}^N$, which is mapped to the physical sampling instants $k = 1, \dots, n_T$ by direct matching or interpolation. The distinction between the sampled physical time k and the numerical time steps n (cf. Sect. 3.2.1) allows one to operate with arbitrary sampling frequencies of the data while controlling the accuracy of the time integration through the choice of the numerical time step h and, when needed, substepping between measurement instants.

The minimisation problem (32) is solved by means of the gradient-descent optimisation algorithm Adam in the Python library PyTorch [68]. Time integration is performed with TorchDiffEq [12] and gradients are evaluated at the converged solutions of the constitutive updates.

The pseudo-code for training is sketched in Algorithm 1 where the explicit notation for the loading protocols is omitted for conciseness. All loading protocols are evaluated in a single batched call by stacking the initial states $\{s_0^{(p)}\}_{p=1}^{n_p}$ and integrating all trajectories in parallel. During training, displacement control is assumed and strain-rate values are computed using finite differences of the strain data at physical times.

3.3.3 Automated selection of internal variables

Depending on the information collected in the training measurements, an accurate prediction of the evolution of the stress may require one or more internal variables in addition to the elastic strain and the mass density. The number of internal variables is chosen via a discrete search over the value of $n_{\alpha} = 0, 1, \dots$ by selecting the smallest dimension of α that guarantees a low (validation) error for a given architecture $(\psi_{\theta}, \mathbb{I}_{\theta})$, see [55]. For each candidate n_{α} , the model is trained by minimising the right-hand side of Eq. (32) and assessed on held-out protocols using the error in the stress predictions. The selected value n_{α}^* is the smallest one such that increasing n_{α} does not yield a significant improvement in the performance to balance accuracy and generalisation. Note that the internal variables are not preassigned physical quantities, with their nature and values being learned end-to-end, but thermodynamic admissibility holds for any value n_{α} , by construction. As a consequence, they provide a latent, energetically consistent parametrisation of material history dependence (cf. Section 3.3.1).

Algorithm 1 Pseudo-code of the training algorithm using a set of stress–strain measurement data at time instances $k = 1, \dots, n_T$ and the initial values for the density. All protocols are evaluated in parallel by stacking initial states, but for clarity, the pseudocode shows a single batch.

Require: Measurement data $\mathcal{D} = \{\bar{\sigma}_k, \bar{\varepsilon}_k, \bar{\rho}_0\}_{k=0}^{n_T}$;

Initial value problem: differentiable integrator `integrate_ivp` (e.g., explicit Euler or implicit schemes) with time step h ;

Neural networks and initial parameters θ : free-energy ψ_θ and transport operator \mathbb{L}_θ ;

Initial conditions: elastic-strain seeds $\varepsilon_0^e \leftarrow \mathbf{0}$ and internal variables $\alpha_0 \leftarrow \mathbf{0}$;

Gradient-descent optimiser `optimiser`($\{\theta, \varepsilon_0^e\}$).

```

1: while training do
2:    $\mathcal{L}_\sigma \leftarrow 0$ ; ▷ initialise cumulative loss
3:    $s_0 \leftarrow (\bar{\rho}_0, \varepsilon_0^e, \alpha_0)$ ;  $\sigma_0 \leftarrow \sigma(s_0; \theta)$ 
4:    $\mathcal{R} \leftarrow (\sigma_0 - \bar{\sigma}_0)$  ▷ compute residual for initial conditions, Eqs. (33)- (31)
5:   for  $n = 0$  to  $N-1$  do
6:      $s_{n+1} \leftarrow \text{integrate\_ivp}(s_n, h; \theta)$  ▷ solve initial value problem, Eqs. (28)
7:   end for
8:   Interpolate  $\{s_n\} \rightarrow \{s_k\}_{k=1}^{n_T}$  ▷ match sampling time
9:   for  $k = 1$  to  $n_T$  do
10:     $\sigma_{\theta,k} \leftarrow \sigma(s_k; \theta)$  ▷ predict stress time-history, Eq. (33)
11:     $\mathcal{L}_\sigma += \|\sigma_k - \bar{\sigma}_k\|_2^2$  ▷ stress loss
12:  end for
13:   $\mathcal{L}_\mathcal{R} \leftarrow \sum_{p=1}^{n_p} \|\mathcal{R}^{(p)}\|_2^2$  ▷ residual loss
14:   $\mathcal{L}_{\text{tot}} \leftarrow \frac{1}{n_p n_T} \mathcal{L}_\sigma + \frac{1}{n_p} \mathcal{L}_\mathcal{R}$ 
15:   $(\theta, \varepsilon_0^e) \leftarrow \text{optimiser}(\{\theta, \varepsilon_0^e\}; \mathcal{L}_{\text{tot}})$  ▷ optimiser step
16: end while
17: return trained network parameters  $\theta^*$ 

```

3.3.4 Inference

After training, the two neural networks ψ_{θ^*} and \mathbb{L}_{θ^*} are employed to infer the material response corresponding to new, unobserved loading protocols. The pseudo-code for inference is sketched in Algorithm 2. At prediction time, the initial conditions for the elastic strain are computed by directly solving for the root of Eq. (31) from the known initial values of the stress, σ_0 , and of the density, ρ_0 , using (quasi-) Newton methods. For displacement-driven protocols, strain-rate values are obtained by finite differences as in the training phase. For full-force or mixed control, unknown strain-rate components are recovered by solving the nonlinear stress-rate residual associated with the protocol via (quasi-)Newton (return-mapping) iterations, with a prescribed relative tolerance of 10^{-6} .

3.3.5 Non-uniqueness of learned representations

The inverse problem of identifying the network parameters θ that minimise Eq. (32) is severely under-determined. For any finite collection of stress trajectories $\bar{\sigma} \in \mathcal{D}$, there exists an infinite family of network parameters and material states that reproduce these data,

$$\mathcal{M}^* = \{(\theta^*, s) \mid \sigma(s; \theta^*) = \bar{\sigma}\}. \quad (34)$$

Among these uncountably many equivalent representations, the optimisation problem (32) is restricted to the physically admissible set $\mathcal{M}_{\text{adm}}^* \subseteq \mathcal{M}^*$ that enforces by construction the conservation of mass and energy, the dissipation inequality, the principle of objectivity, and the material stability.

Since the optimisation in (32) is restricted to $\mathcal{M}_{\text{adm}}^*$, the trained network delivers a well-posed and thermodynamically consistent mapping $s \mapsto \sigma(s; \theta^*)$ for any admissible loading path. The pair $(\psi_{\theta^*}, \mathbb{L}_{\theta^*})$ should therefore be interpreted as one admissible constitutive representation, rather than the unique material law. The same caveat applies to the identified elastic strain and internal variables, whose values additionally depend on the specified initial conditions (cf. Sect. 3.3.1). The initial elastic strain follows the root-finding problem (31) which is well-posed for a given θ^* under the conditions considered, while all internal variables are initialised to zero. This choice deliberately avoids the phenomenological assumptions often adopted in conventional constitutive modelling and ensures a well-posed identification of the state space when no microstructural information is available.

Note that the framework can be extended to discover internal variables from the internal structure of materials. When richer measurements are available – for instance, topological descriptors or internal degrees of freedom of the material

microstructure – the admissible set $\mathcal{M}_{\text{adm}}^*$ can be further restricted by linking the internal variables to those data, following the methodology proposed in [54–56].

Algorithm 2 Pseudo-code of the inference algorithm relying on the trained network parameters θ^* , the initial values for stress and density, and the strain time-history or force control.

Require: Measured strain histories $\{\bar{\epsilon}_k\}$ (or stress control $\{\bar{\sigma}_k\}$), initial stresses σ_0 , initial density ρ_0 ;
 Root-finding solver `root_solver`, initial-value-problem routine and method `integrate_ivp` and time step h ;
 Trained parameters θ^* (neural networks $\psi_{\theta^*}, \mathbb{L}_{\theta^*}$).

- 1: Initialise guess $s_0 \leftarrow (\rho_0, \mathbf{0}, \mathbf{0})$
- 2: $s_0 \leftarrow \text{root_solver}(\mathcal{R}(s_0, \sigma_0; \theta^*))$ ▷ root-finding (elastic strain), Eq. (31)
- 3: **for** $n = 0$ **to** $N-1$ **do**
- 4: $s_{n+1} \leftarrow \text{integrate_ivp}(s_n, h; \theta^*)$ ▷ solve initial value problem, Eqs. (28)
- 5: $\sigma_{n+1} \leftarrow \sigma(s_{n+1}; \theta^*)$ ▷ predict stress
- 6: **end for**
- 7: **return** stress time-histories $\{\sigma_n\}_{n=0}^N$ and state trajectories $\{s_n\}_{n=0}^N$

4 Synthetic benchmarks: identification of constitutive equations

The performance and accuracy of the proposed methodology are investigated and quantified relying on synthetic measurement data. The latter involve datasets generated from analytical material laws of progressively higher complexity, i.e., elasto- and hypo-plasticity, including rate and hardening effects, and non-associative plastic flow rules. Having exact knowledge of the ground truth, i.e., the constitutive model that underlies the data, these tests allow a strict, quantitative evaluation of the methodology in identifying consistent and reliable constitutive equations from data and inferring unobserved material responses. The benchmarks enable not only to assess the accuracy of stress predictions, but also to evaluate the identified free-energy and dissipation functions, as well as the evolution of automatically discovered internal variables. To highlight the benefit of enforcing non-equilibrium thermodynamics as hard constraints, no prior information about internal variables is used following the automatic selection procedure detailed in Section 3.3.3.

The considered synthetic datasets mimic standard laboratory protocols, typically comprising monotonic loading followed by an unloading phase. For each protocol, only stress–strain pairs are sampled. Here, density is assumed constant and the identification focuses on the inelastic evolution. The initial value problem, Eq. (28), is integrated over a unit pseudo-time interval using an explicit scheme (explicit Euler), with step size $h = 0.004$, i.e., 250 steps per protocol.

For completeness, Appendix B provides a comparison of the present hard-constrained framework with learning formulations using soft constraints for the dissipation inequality.

4.1 One-dimensional benchmarks

The first set of benchmarks involves the following one-dimensional material laws: elasto-plasticity (EP), hypo-plasticity (HP), elasto-visco-plasticity with Perzyna-type viscosity (EVP), and elasto-plasticity with isotropic hardening (EPH).

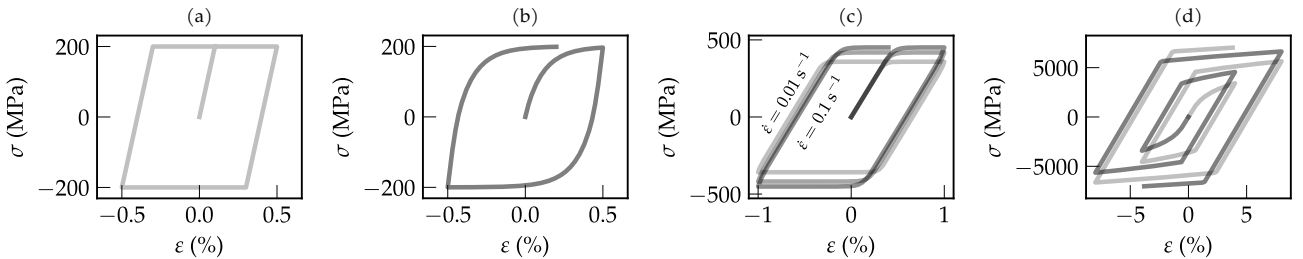


Figure 2: Loading protocol and stress data for the one-dimensional benchmarks used for training. From left to right: (a) elasto-plastic (EP), (b) hypo-plastic (HP), (c) elasto-visco-plastic (EVP), and (d) elasto-plastic with isotropic hardening (EPH) material.

4.1.1 Elasto-plasticity

The first example concerns an idealised elastic, perfectly plastic material. The stress depends only on the elastic strain, $\sigma = E \varepsilon^e$, with yield condition $|\sigma| \leq \sigma_y$. The material has elastic modulus $E = 200$ GPa and yield stress $\sigma_y = 200$ MPa.

Data and training The training set consists of one protocol with sequential loading-unloading-reloading at constant strain-rate amplitude $|\dot{\varepsilon}| = 0.01$ s⁻¹, see Figure 2. The free-energy network ψ_θ has two hidden layers with 64 units and exponential-linear-unit (ELU) activation; the transport-operator network \mathbb{L}_θ has three hidden layers with 64 units and leaky-rectified linear unit (LReLU) activation. The training loss without considering internal variables converges after ~ 3000 epochs, with a mean absolute error in the stress predictions below 0.1%.

Results Figure 3 compares the predictions at inference with the ground-truth results for two unobserved loading paths: (i) strain cycles of increasing amplitude and (ii) stress cycles of fixed amplitude. Figure 3 (a) shows the stress-strain response, (b) the time evolution of the stress, (c) the evolution of the inferred free energy with respect to the identified elastic strain, and (d) the dissipation rate versus the inferred plastic strain rate. The free-energy and dissipation rate are reported considering a unit constant reference volume, unless stated otherwise.

Under strain cycling (Fig. 3, top), the neural material model reproduces the onset of yielding at the expected elastic threshold $\sigma_y/E = 0.1\%$ and the subsequent perfectly plastic response, including the characteristic stress plateau and the return to the same elastic slope upon unloading. The size of the elastic domain and the plastic flow direction remain consistent across cycles, and the predicted plastic strain rate, free energy and dissipation rate match the reference evolution.

For stress cycles of fixed amplitude with $\max |\sigma| < \sigma_y$ (Fig. 3, bottom), the model correctly predicts a purely reversible elastic response with closed (σ, ε) loops, vanishing plastic strain rates, and zero dissipation, see Figure 3 (c,d). These results show that, even when trained on a single simple protocol and stress-only data, hard thermodynamic constraints enable generalisation of both the macroscopic response and the thermodynamic fields to loading modes not seen during training, including the correct identification of the degree of homogeneity of the dissipation rate function with respect to the plastic strain rate, cf. Fig. 3 (d).

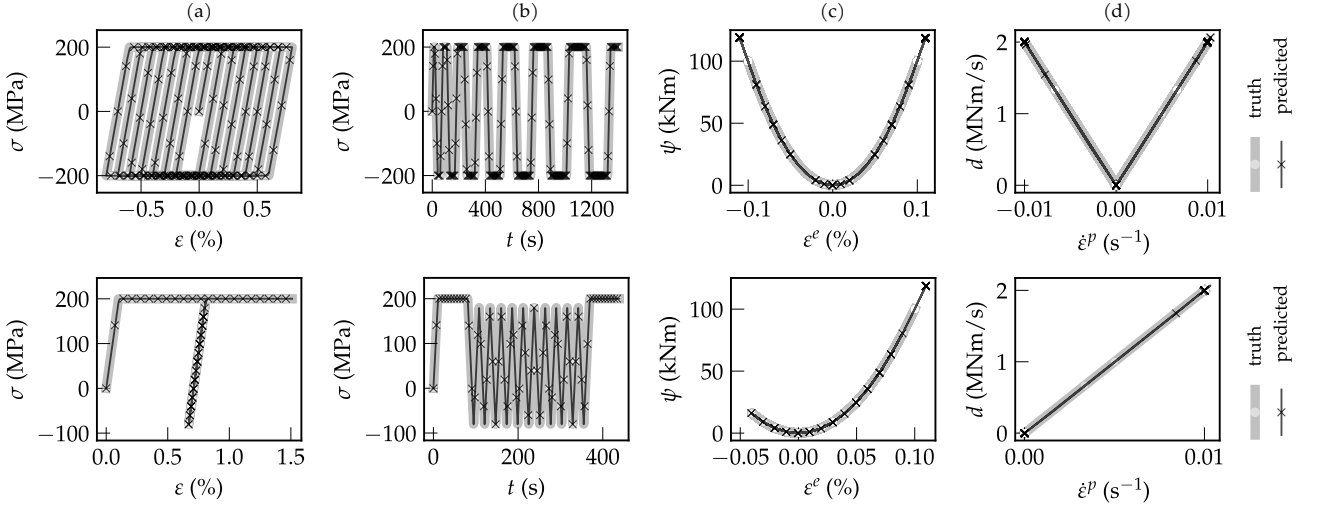


Figure 3: Predictions at inference of the response of the elasto-plastic (EP) material under unobserved loading protocols: increasing-amplitude cyclic test (top) and stress cycles of fixed amplitude (bottom). From left to right: (a) stress versus strain ($\sigma - \varepsilon$), (b) stress versus time ($\sigma - t$), (c) free-energy density versus elastic strain ($\psi - \varepsilon^e$), and (d) dissipation rate versus plastic strain rate ($d - \dot{\varepsilon}^p$). The free energy is reported considering a unit constant reference volume.

4.1.2 Hypo-plasticity

The second example considers a hypo-plastic material model with emerging ratcheting [46] governed by the nonlinear stress-rate equation $\dot{\sigma} = E\dot{\varepsilon} + E(\sigma/\sigma_y)^s|\dot{\varepsilon}|$, where the elastic modulus and yield stress are kept the same as in the first benchmark and $s = 0.5$ expresses the nonlinearity of the hypo-plastic formulation. In contrast to elasto-plasticity, hypo-plasticity does not rely on elastic-plastic strain-rate decomposition. Moreover, the plastic flow rule cannot be cast as the (sub-)differential of a convex dissipation potential (cf. [21]). These aspects make this simple case a stringent test for the proposed methodology.

Data and training The training set, loading protocol, and network architecture are kept identical to those of the elasto-plastic benchmark, see Figure 2.

Results Figure 4 shows the predictions and the reference results for the hypo-plastic material model for the same two families of unobserved paths as for the case of the elasto-plastic model. The neural model attains high accuracy in terms of the stress and the inferred elastic strain, free-energy, plastic-strain rate, and dissipation rate.

Under strain cycling of increasing amplitude, the predicted (σ, ε) trajectories show that the tangent stiffness evolves smoothly with the stress level, consistent with the nonlinear rate equation. The dissipation rate remains strictly positive, reflecting the non-recoverable character of the response, and the inferred elastic strain and free energy evolve consistently throughout the cycles.

Under stress cycling, the network captures the hallmark of hypo-plasticity, ratcheting, i.e., the progressive, non-hysteretic accumulation of strain with each cycle. The model reproduces the gradual drift in total strain and the open (σ, ε) trajectories associated with ratcheting. The predicted behaviour demonstrates that the learned neural operator moves beyond the assumptions of dissipation potentials and robustly represents all hypo-plastic features.

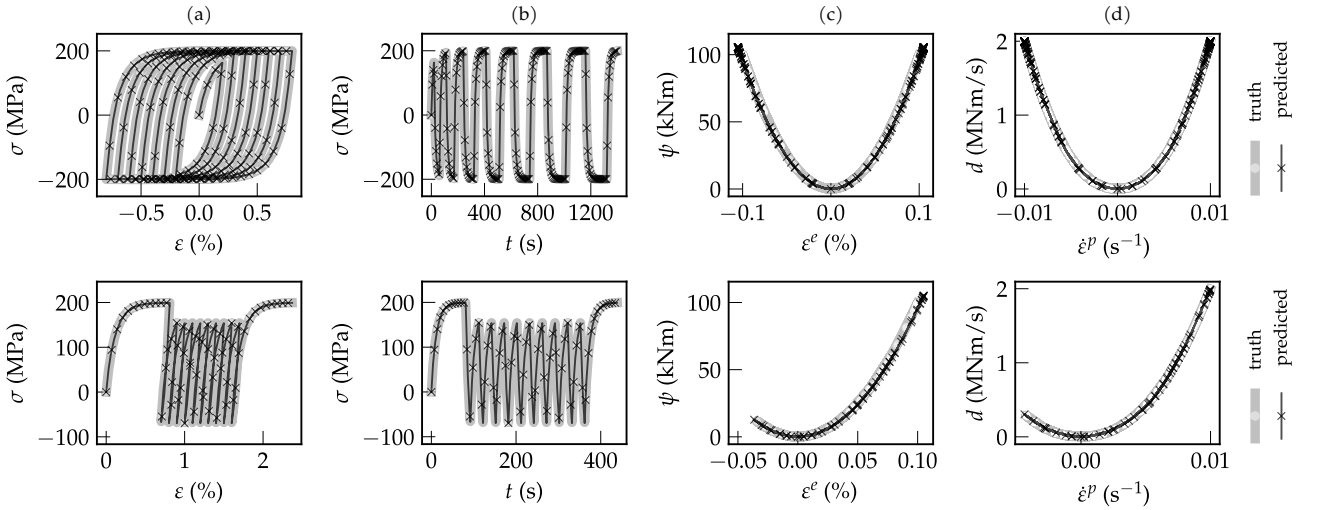


Figure 4: Predictions at inference of the response of the hypo-plastic (HP) material under unobserved loading protocols: increasing-amplitude cyclic test (top) and stress cycles with ratcheting (bottom). From left to right: (a) stress versus strain ($\sigma - \varepsilon$), (b) stress versus time ($\sigma - t$), (c) free-energy density versus elastic strain ($\psi - \varepsilon^e$), and (d) dissipation rate versus plastic strain rate ($d - \dot{\varepsilon}^p$).

4.1.3 Rate dependence

The third benchmark builds upon the elasto-plastic formulation of the first benchmark by further introducing rate dependence through Perzyna’s overstress law (see [75]). The elastic modulus and yield stress are equal to 100 GPa and 200 MPa, respectively, and are complemented with the viscosity parameter equal to 1 GPa/s and the rate-sensitivity dimensionless exponent, set equal to 5.

Data and training The training set consists of one protocol with a sequence of loading-unloading-reloading at three different constant strain-rate amplitudes $|\dot{\varepsilon}| = 0.01, 0.05, \text{ and } 0.1\% \text{ s}^{-1}$, see Figure 2. The neural network architecture is the same as for the previous benchmarks.

Results Figure 5 showcases the predictions of the neural model under a velocity-stepping sequence followed by a hold at zero strain rate, none of which appeared in training. The neural model recovers the expected rate sensitivity: larger $|\dot{\varepsilon}|$ yields larger overstress, with stress levels and plastic strain-rate values correctly matching the reference response across all steps. During the hold phase, the model captures stress relaxation toward the yield value, a concomitant decay of the plastic strain rate, and the vanishing of the dissipation rate.

The inferred state variable, ε^e , also matches the reference model, during both the rate transitions and the relaxation. The same holds for the free energy. The results indicate that the learned dynamics encode the correct rate-overstress coupling and generalise to relaxation phenomena absent from the training data.

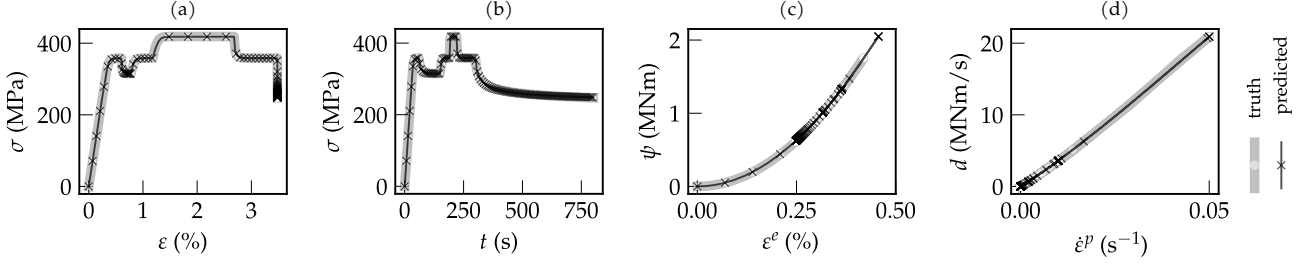


Figure 5: Predictions at inference of the response of the elasto-visco-plastic (EVP) material under velocity stepping and subsequent hold test, i.e., $\dot{\varepsilon} = \{0.01, 0.002, 0.01, 0.05, 0.0\} \text{ s}^{-1}$. From left to right: (a) stress versus strain ($\sigma - \varepsilon$), (b) stress versus time ($\sigma - t$), (c) free-energy density versus elastic strain ($\psi - \varepsilon^e$), and (d) dissipation rate versus plastic strain rate ($d - \dot{\varepsilon}^p$).

4.1.4 Elasto-plasticity with hardening

The fourth benchmark considers an elasto-plastic constitutive law with Ramberg-Osgood isotropic hardening [70], with yield condition $|\sigma| \leq \sigma_y + C(\varepsilon_c^p)^m$, where ε_c^p is the cumulative plastic strain, $C = 10 \text{ MPa}$ the hardening modulus, and $m = 0.3$ the hardening exponent. The elastic modulus and yield strength are $E = 200 \text{ GPa}$ and $\sigma_y = 200 \text{ MPa}$.

Data and training The training set consists of two protocols with sequential loading-unloading phases at a constant strain-rate amplitude $|\dot{\varepsilon}| = 0.002 \text{ s}^{-1}$, see Figure 2. The network architecture remains unchanged. An initial run assumes a state space spanned solely by the elastic strain. Under this assumption, the mean absolute percentage error stagnates at $\approx 142\%$ after a few hundred epochs, indicating that a single-variable state is insufficient to represent isotropic hardening (cf. Sect. 3.3.3). Training is then repeated introducing a scalar internal variable α , learned end-to-end without a prescribed interpretation. With this modification, the mean absolute error decreases to $\approx 0.2\%$, confirming that one internal variable is enough to capture the observed material response.

Results Figure 6 evaluates the generalisation of the neural model to an unseen multi-cycle path. The model reproduces the defining features of isotropic hardening with the progressive expansion of the yield level with accumulated plastic strain. The dissipation rate versus plastic strain rate ($d - \dot{\varepsilon}^p$, panel b) curves agree closely with the reference model and minor discrepancies are limited to a few localised points near load reversals. The automatically identified internal variable α behaves as a scalar hardening measure, nearly monotone during plastic flow and ordering the cycles by the expansion of the elastic domain, correlating strongly with the cumulative plastic strain ε_c^p (cf. panels c, d).

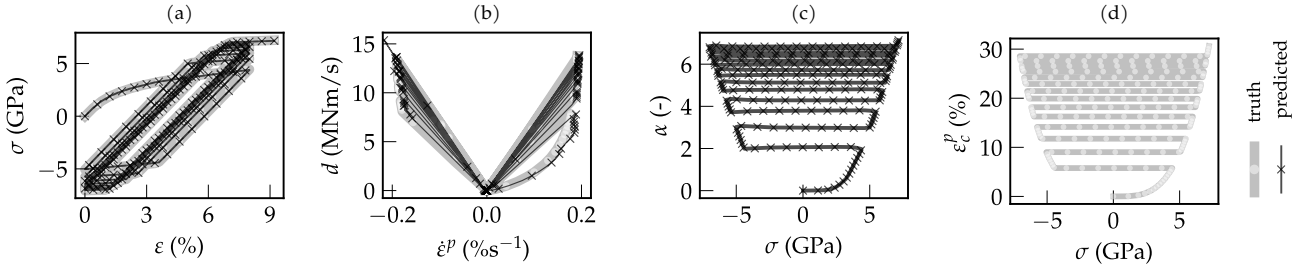


Figure 6: Predictions at inference of the response of the elasto-plastic material with isotropic hardening (EPH) under an unobserved cyclic loading protocol with multiple loading and unloading sequences. From left to right: (a) stress versus strain ($\sigma - \varepsilon$), (b) dissipation rate versus plastic strain rate ($d - \dot{\varepsilon}^p$), (c) automatically-identified internal variable α and (d) cumulative plastic strain ε_c^p versus stress.

Figure 7 presents the inferred free-energy density. At $\alpha = \varepsilon_c^p = 0$, the energy closely matches the reference elastic energy (panel a). The learned surface $\psi(\varepsilon^e, \alpha)$ increases with both $|\varepsilon^e|$ and α , yielding stresses consistent with the hardening observed in Fig. 6. A small asymmetry in the free energy with respect to the elastic strain is observed (panel c), but the predictions at inference remain physically consistent, indicating that the model has discovered an interpretable hardening variable and a consistent free-energy landscape from stress-only training data.

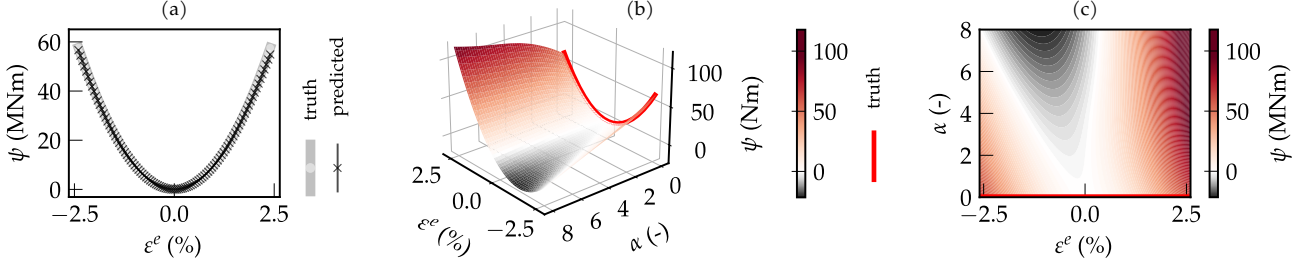


Figure 7: Predictions at inference of the response of the elasto-plastic material with isotropic hardening (EPH) in terms of the free-energy density ψ . From left to right: (a) comparison between predictions and ground truth for $\alpha = 0$ and zero cumulative plastic strain, respectively, and (b-c) predicted energy as a function of the elastic strain and the identified internal variable.

4.2 Three-dimensional non-associative benchmark

The last benchmark showcases a three-dimensional, incrementally nonlinear, elasto-plastic, non-associative Drucker–Prager material with constant density (cf. [21]). The material parameters are: bulk modulus $K = 46.7$ MPa, shear modulus $G = 40$ MPa, friction and dilatancy coefficients equal to 1.0 and 0.5, respectively, and seismic parameter equal to 100.

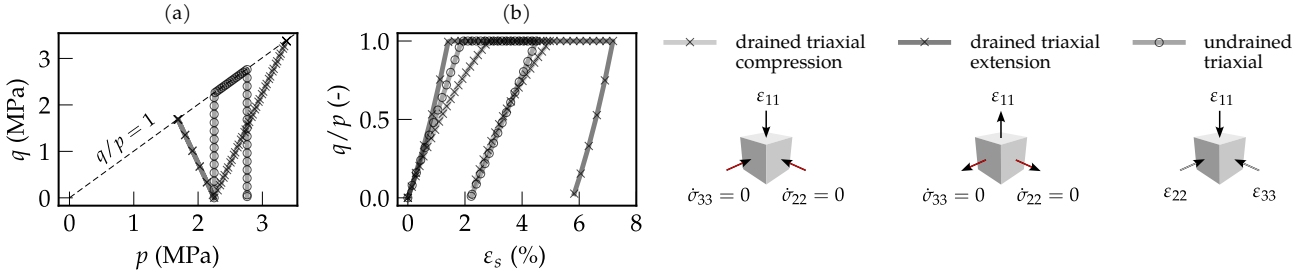


Figure 8: Loading protocols for the training process in terms of (a) deviatoric versus volumetric stress ($q - p$) and (b) friction versus deviatoric strain ($q/p - \epsilon_s$). The measurement data include: drained triaxial compression/extension (ϵ_{11} prescribed, $\dot{\sigma}_{22} = \dot{\sigma}_{33} = 0$) and (isochoric) undrained triaxial compression (ϵ_{11} prescribed, $\epsilon_{22} = \epsilon_{33} = -\frac{\epsilon_{11}}{2}$) at different initial confining pressures p .

The neural constitutive equations are formulated through a reduced set of invariant representations of the stress and strain, i.e., $\boldsymbol{\sigma} = (p, q)$ and $\boldsymbol{\varepsilon} = (\varepsilon_v, \varepsilon_s)$, namely $p = -1/3 \text{tr}(\boldsymbol{\sigma})$, $q = \sqrt{3/2} \boldsymbol{\sigma}' : \boldsymbol{\sigma}'$, $\varepsilon_v = -\text{tr}(\boldsymbol{\varepsilon})$, $\varepsilon_s = \sqrt{2/3} \boldsymbol{\varepsilon}' : \boldsymbol{\varepsilon}'$, with $\boldsymbol{\sigma}' = \boldsymbol{\sigma} + p\mathbf{I}$ and $\boldsymbol{\varepsilon}' = \boldsymbol{\varepsilon} + \varepsilon_v\mathbf{I}/3$ the deviatoric tensors, with compressive stress and strain taken as positive.

Data and training Training data are generated by single loading-unloading paths, as in conventional laboratory testing. From an initially unstressed state ($\boldsymbol{\sigma} = \mathbf{0}$), isotropic compression first creates admissible states at several confining pressures ($0.5 \leq p \leq 2$ MPa, $q = 0$ MPa). These states then serve as initial conditions for drained triaxial compression/extension and undrained triaxial compression tests, depicted in Figure 8), with strain rates of order $0.3\text{--}1 \times 10^{-3} \text{ s}^{-1}$.

The free-energy network ψ_θ uses three hidden layers with 64 nodes and ELU activation and the transport-operator network \mathbb{L}_θ uses four hidden layers with 64 nodes and Softplus activation. The material state is assumed to be spanned by the elastic strain only. With this choice, the training loss converges in approximately 5000 epochs to a mean absolute error in the stress predictions below 0.1%, indicating that no additional internal variables are required.

Results Predictions at inference are tested for an unseen mixed-control, cyclic path, i.e., simple shear, where ε_{12} is prescribed and normal stresses are kept constant from an initial confining pressure $p = 2$ MPa. The stress-control condition (constant p) is enforced at every step by Newton–Raphson iterations with the neural material model.

Figure 9 shows the predictions in terms of the shear stress, dissipation rate, and volumetric strains. The friction response q/p versus the shear strain ε_s matches the reference results over the repeated loading–unloading cycles (panel a). The dissipation versus plastic–shear rate relationship $d-\dot{\varepsilon}_s^P$ (panel b) is strictly non-negative and scales with $|\dot{\varepsilon}_s^P|$ as expected for a rate-independent plastic flow with only limited discrepancies with respect to the reference model near load reversals. The predicted volumetric–shear trajectories (panels c–d) demonstrate the ability of the framework to recover the inherent non-associative behaviour. The plastic volumetric–shear strain trajectory displays a slope consistent

with the nominal dilatancy coefficient (0.5) in contrast with a purely associative flow which is included for reference. Non-associativity is recovered naturally from the data and the identified transport operator provides a general evolution law with thermodynamic admissibility guaranteed by construction.

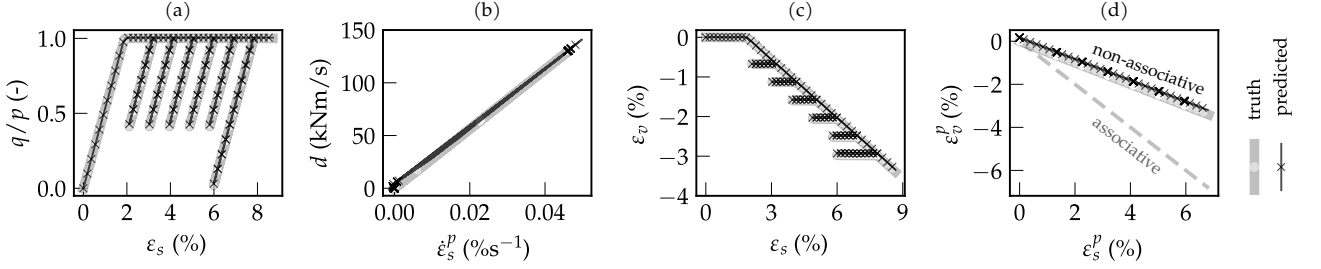


Figure 9: Predictions at inference for an unobserved protocol (simple shear, i.e., ε_{12} prescribed, $\dot{\sigma}_{11} = \dot{\sigma}_{22} = \dot{\sigma}_{33} = 0$) with multiple loading-unloading sequences. From left to right: (a) friction versus shear strain ($q/p - \varepsilon_s$), (b) dissipation rate versus shear plastic strain rate ($d - \dot{\varepsilon}_s^p$), (c) volumetric versus shear strain ($\varepsilon_v - \varepsilon_s$), and (d) volumetric versus shear plastic strain ($\varepsilon_v^p - \varepsilon_s^p$).

Figure 10 compares the identified thermodynamic fields with their analytical counterparts, namely the free-energy density (top) and the dissipation rate (bottom). The inferred free energy ψ is convex in the elastic strains by construction. For elastic-strain magnitudes up to $\sim 1\%$, it coincides with the reference values. For larger magnitudes, small deviations appear (relative error within $\approx 2\%$), consistent with a slight offset in the effective elastic moduli relative to the nominal (K, G). However, note that this does not affect the stress predictions, since by construction $\sigma = \partial\psi/\partial\varepsilon^e$ keeps the stress and elastic strain thermodynamically consistent. The learned and reference dissipation rate are presented in Figure 10 (bottom) considering a field of admissible stress states (p, q) under an undrained-triaxial loading with constant strain rate. The dissipation rate is everywhere non-negative and its magnitude increases as q/p approaches 1 (yield locus). This demonstrates that the neural model automatically captures the underlying Mohr-Coulomb criterion. Quantitatively, the percentage relative error stays below $\sim 0.6\%$ with largest deviations confined near the yield locus where the inferred dissipation is slightly higher than the reference.

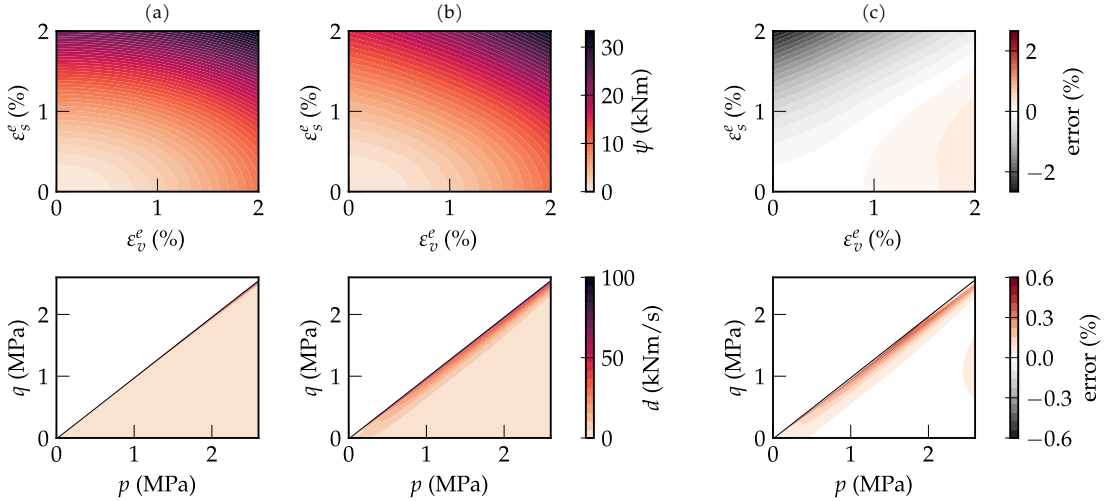


Figure 10: Ground-truth and learned free energy function (top) and dissipation rate (bottom). From left to right: (a) true and (b) learned free energy (top) and dissipation rate (bottom); (c) percentage relative error for the free energy (top), $(\psi_\theta - \bar{\psi})/\bar{\psi}_{\max}$ %, and dissipation rate (bottom), $(d_\theta - \bar{d})/\bar{d}_{\max}$ %, where ψ_θ and d_θ are the predictions, $\bar{\psi}$ and \bar{d} are the analytical values, and the subscript max denotes the maximum value. The values of the dissipation rate refer to an undrained triaxial loading with constant strain rate equal to $0.3 \cdot 10^{-3} \text{ s}^{-1}$.

The framework identifies an objective, thermodynamically consistent, and explicitly non-associative Drucker–Prager response from standard triaxial measurements and extrapolates reliably to a qualitatively different loading mode (simple shear) under mixed stress–strain control, delivering consistent predictions for stress, flow direction, free energy, and dissipation.

5 Application to granular materials: discovery of constitutive equations

Granular media are an excellent candidate to test the performance of the present learning framework, as they are heterogeneous materials that exhibit a rich, complex, and history-dependent behaviour. Classical quasi-static material models rely on heuristic plasticity and critical-state theory (e.g., state-dependent friction, dilatancy relations [1, 47, 73, 76, 77]), yet they remain hindered by the phenomenological choices of the state variables and underlying constitutive relations, which are often tuned by human trial-and-error adjustments. Despite the progress enabled by in-operando testing [44, 78, 80], no universally accepted closed-form law exists for granular materials, particularly across transitional regimes (e.g., quasi-static to dynamic) and under cyclic, non-proportional loading paths.

Here, the learning framework is applied to the discovery of constitutive equations for a dry, cohesionless granular material under virtual testing conditions that mimic conventional laboratory settings. Laboratory data typically reflect a combination of (i) aleatoric (statistical) uncertainty from the material’s inherent heterogeneity, (ii) epistemic uncertainty arising from incomplete knowledge of the material state and boundary conditions, and (iii) measurement errors. These challenges are often exacerbated by sparse coverage of the state/parameter space (few tested protocols and initial conditions) and limited temporal resolution. In the present work, attention is primarily focused on aleatoric and epistemic sources of uncertainty.

Physical tests are replaced by in silico experiments using the Discrete Element Method (DEM) to generate high-fidelity numerical analogues of the material response [16]. DEM resolves the micro-mechanical and geometrical complexity of the material, allowing the emergent constitutive behaviour to arise naturally from particle interactions without prescribing macro-mechanical laws. Consequently, aleatoric variability originates from the spatial heterogeneity in both material properties and microstructural topology. Epistemic uncertainty is associated with the limited observability of the internal material state (e.g., fabric, force chains) in conventional laboratory settings and the practical opacity of accessing grain-scale kinematics and dynamics. Although DEM provides full access to grain-scale information, this study deliberately restricts the measurement data to macroscopic observables readily available in laboratory tests: stress–strain pairs and the initial mass density. The unobserved grain-scale information is therefore treated as epistemic.

5.1 Discrete element method and in silico experiments

The reference granular material is modelled as an assembly of spherical discrete-element particles. The particles interact with each other through frictional contact laws and their motion is governed by Newton’s laws of motion. The numerical experiments are conducted using the open-source software YADE-Open DEM [48, 56], where the equations of motion are integrated in time explicitly using a central finite difference algorithm.

The analogue material is a purely frictional granular medium. The adopted particle properties define an effective DEM analogue of a dry, cohesionless granular assembly under quasi-static loading. Each grain is assigned a diameter d , a mass density $\rho_s = 2600 \text{ kg/m}^3$, and an effective elastic behaviour defined by a Young’s modulus $E = 60 \text{ MPa}$ and a Poisson ratio $\nu = 0.5$. Grains interact through Coulomb friction interfaces with friction coefficient $\mu = 0.5$. The grain-size distribution is sampled from a uniform law $d \sim d_{50}\mathcal{U}(0.5, 1.5)$, with median diameter $d_{50} = 10 \text{ }\mu\text{m}$.

The present application is restricted to quasi-static deformation regimes, by keeping the dimensionless inertial number $I = \dot{\gamma}d_{50}\sqrt{\rho/p}$ below a value of 10^{-4} [27], where $\dot{\gamma}$ is the shearing rate, d_{50} the median particle diameter, ρ the mass density, and p the confining pressure. To limit boundary effects and satisfy the Hill–Mandel condition, the simulated granular packings employ periodic boundary conditions [65].

Let V be a material element, under periodic boundary conditions and quasi-static conditions. The volume-averaged Cauchy stress is given by the Love–Weber expression [51, 83]:

$$\sigma_V \equiv \frac{1}{|V|} \int_V \sigma(\mathbf{x}) \, d\mathbf{x} = \frac{1}{|V|} \sum_c \mathbf{f}_c \otimes \mathbf{l}_c, \quad (35)$$

where $|V|$ is the volume, \mathbf{f}_c is the contact force, and \mathbf{l}_c the branch vector, with summation over all contacts c in the assembly. The average strain rate and strain are directly obtained from the boundary deformation of the periodic cell. Under periodic boundary conditions, the dissipation inequality (6) can be reformulated in terms of average quantities

$$d_V = \sigma_V : \dot{\epsilon}_V - \rho_V \dot{\psi}_M \geq 0, \quad (36)$$

where subscript V denotes volume averages, e.g. $\sigma_V = \frac{1}{|V|} \int_V \sigma(\mathbf{x}) \, d\mathbf{x}$, and subscript M denotes mass-weighted averages, e.g., $\dot{\psi}_M = \frac{1}{M} \int_V \rho(\mathbf{x}) \dot{\psi}(\mathbf{x}) \, d\mathbf{x}$, with $M = \int_V \rho(\mathbf{x}) \, d\mathbf{x}$ representing the total mass and $\mathbf{x} \in V$ the spatial coordinates. Note that, under the assumption of infinitesimal strains, time differentiation commutes with the averaging operators. Exploiting

the formalism presented in Section 2, inequality (36) provides equivalent state laws for the chemical potential, energetic stress, and driving forces, namely

$$\mu_V \equiv \rho_V \frac{\partial \psi_M}{\partial \rho_V}(\rho_V, \boldsymbol{\varepsilon}_V^e, \boldsymbol{\alpha}_V), \quad \boldsymbol{\sigma}_V^e \equiv \rho_V \frac{\partial \psi_M}{\partial \boldsymbol{\varepsilon}_V^e}(\rho_V, \boldsymbol{\varepsilon}_V^e, \boldsymbol{\alpha}_V), \quad \mathcal{A}_V^e = -\mathcal{A}_V^d \equiv \rho_V \frac{\partial \psi_M}{\partial \boldsymbol{\alpha}_V}(\rho_V, \boldsymbol{\varepsilon}_V^e, \boldsymbol{\alpha}_V). \quad (37)$$

This results in equivalent expressions for the material stress and evolution equations

$$\boldsymbol{\sigma}_V = \boldsymbol{\sigma}_V^e - \rho_V \mu_V \mathbf{I}, \quad \mathbf{z}_V = \mathbb{L}_V \boldsymbol{\mathcal{Y}}_V, \quad (38)$$

under the assumption of a negligible dissipative stress. The volume-averaged generalised fluxes and forces, \mathbf{z}_V and $\boldsymbol{\mathcal{Y}}_V$, collect the rates of the material-averaged irreversible strain and internal variables and the averaged generalised forces, respectively. Meanwhile, \mathbb{L}_V acts as an equivalent transport operator, whose symmetric component must be positive semi-definite to fulfil the dissipation inequality. For conciseness, the subscripts M and V are removed henceforth and all quantities are considered volume averages, except for the free energy which is considered as mass-weighted average.

The macroscopic stress response extracted from DEM may exhibit fluctuations due to finite-size effects and evolving contact networks. In the following, this variability is treated as part of the observed macroscopic response (aleatoric uncertainty) and the learning task is performed on ensembles of independent realisations of the material, rather than attempting to identify or track grain-scale state variables.

5.1.1 In silico experiments

Granular packings are generated by first creating random clouds of spherical particles, initially with no active contacts, enclosed in a three-dimensional periodic cell. The assembly is then isotropically consolidated to prescribed stress conditions. During this preparation stage, the friction coefficient is temporarily reduced to a value μ_c , with $0 \leq \mu_c \leq \mu$, in order to control compaction and densification of the packing, with smaller μ_c values producing denser packings.

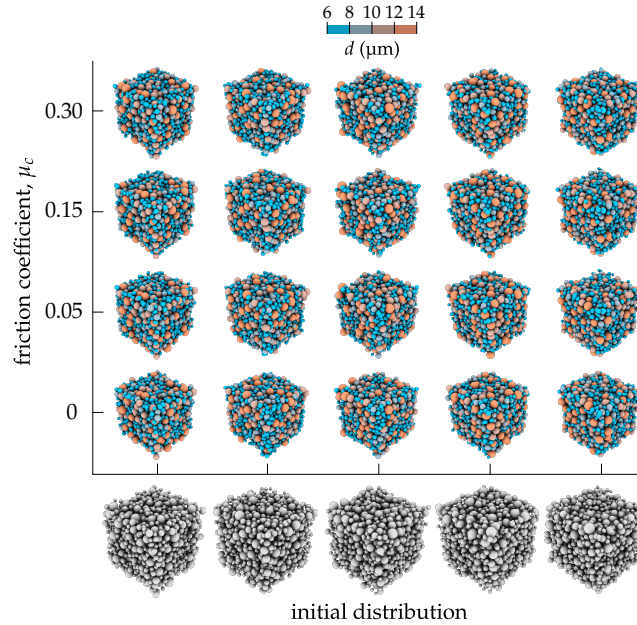


Figure 11: Sample generation: (i) creation of random particle clouds with different seeds (horizontal axis) and (ii) compaction with different values of the friction coefficient μ_c to control the degree of densification (vertical axis). Five randomly sampled particle clouds are considered. Each cloud is subjected to isotropic consolidation (up to $p = 100$ kPa) considering four different values of μ_c , resulting in 20 different samples, with the same particle-size distribution.

Five independent random particle clouds are generated using different seeds. For each cloud, four different values of the preparation friction $\mu_c \in \{0, 0.05, 0.15, 0.30\}$ are considered to mimic the aleatoric variability of the material. This procedure yields 20 realisations of the same granular material, all sharing the same particle-size distribution but exhibiting different microstructures and solid fractions ρ/ρ_s , see Figure 11.

Consolidation of the particle clouds proceeds to a homogeneous mean effective stress $p = 100$ kPa and zero deviatoric stress $q = 0$ kPa, after which the contact friction is reset to its nominal value $\mu = 0.5$. Each packing is then subjected to

(i) isotropic extension to generate states at different confining pressures $p \in \{20, 40, 60, 80, 100\}$ kPa, see Figure 12. The resulting isotropic states, with confining pressure $0 \leq p \leq 100$ kPa and solid fraction $0.6 \leq \rho/\rho_s \leq 0.7$, serve as initial conditions for drained triaxial compression tests, see Figure 13. These tests include: (ii) monotonic loading up to a total axial strain of approximately 15%, (iii) monotonic loading to 4% axial strain followed by unloading to $q = 0$, and (iv) monotonic loading to 12% axial strain followed by unloading to $q = 0$. Note that the presence of non-monotonic loading paths enables the assessment of the method’s ability to distinguish between loading and unloading paths. However, neither reloading nor cyclic loading are considered in the generation of the datasets used in the training process.

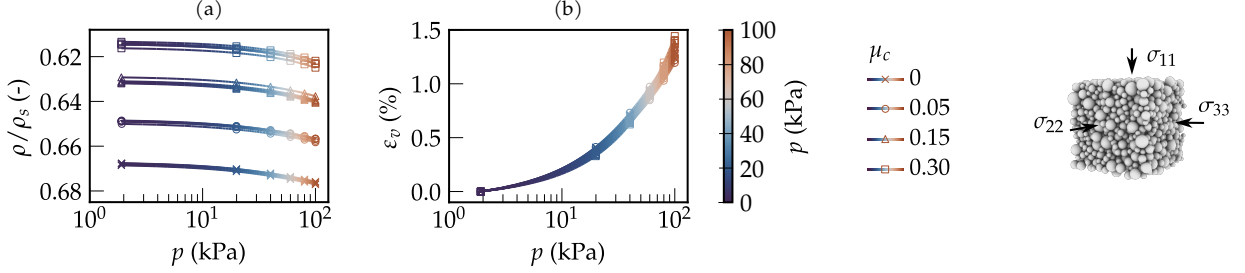


Figure 12: Isotropic extension loading protocols for the training process in terms of (a) solid fraction versus isotropic pressure ($\rho/\rho_s - p$) and (b) volumetric strain versus isotropic pressure ($\varepsilon_v - p$). The measurement data include stress-strain pairs and initial density for five different microstructural realisations at $p = 100$ kPa, obtained from four different values of the inter-particle friction coefficient μ_c .

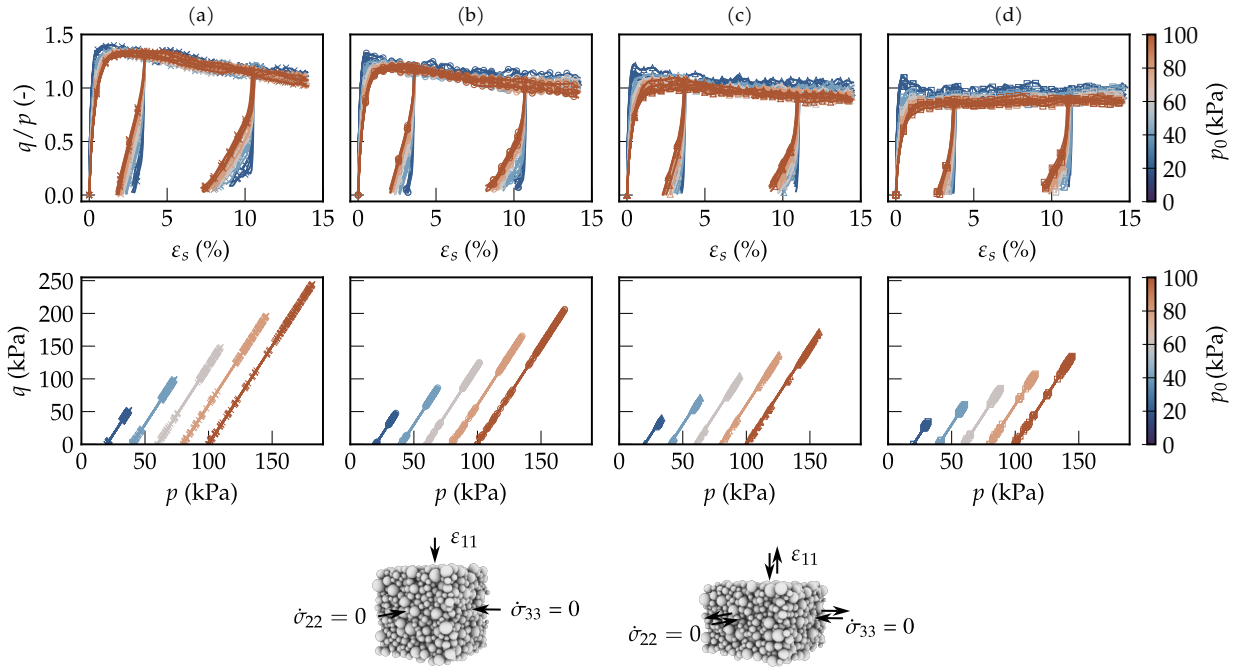


Figure 13: Drained triaxial protocols for the training process in terms of (top) deviatoric stress versus strain ($q - \varepsilon_s$) and (bottom) deviatoric versus isotropic stress ($q - p$) for samples generated using a friction coefficient μ_c equal to (a) 0, (b) 0.05, (c) 0.15, and (d) 0.3. The measurement data include: (i) monotonic triaxial compression (ε_{11} prescribed, $\dot{\sigma}_{22} = \dot{\sigma}_{33} = 0$) up to $\varepsilon_s \sim 15\%$, and triaxial compression up to (ii) $\varepsilon_s \sim 4\%$ and (iii) $\varepsilon_s \sim 12\%$ followed by unloading up to approximately zero deviatoric stress, at different initial confining pressures $p \in (20, 40, 60, 80, 100)$ kPa.

5.2 Learning an effective constitutive model from macroscopic data

The learning task uses only labelled volume-averaged strain–stress histories and the initial value for the density, as in Section 3.3, for both the monotonic isotropic extension tests and the (non-)monotonic triaxial tests, cf. Figures 12–13.

Stress and strain are expressed through the reduced invariant representations (p, q) and $(\varepsilon_v, \varepsilon_s)$, respectively, which are sufficient for the axisymmetric stress states covered by the triaxial protocols.

Both the free-energy network ψ_θ and the transport-operator network \mathbb{L}_θ are implemented as feed-forward neural networks with three hidden layers, 64 neurons per layer, and Softplus activation functions. The governing initial value problem is integrated using an explicit midpoint scheme, with step size $h = 0.0025$, i.e., 400 steps per protocol.

Initial conditions are treated in a way that mirrors the hierarchical structure of the data. At the reference isotropic state $(p, q) = (100 \text{ kPa}, 0)$, the unknown elastic strain is determined for each realisation by solving Eq. (31), with $\alpha_0 = \mathbf{0}$. The remaining initial states are handled by a shooting strategy, with time integration performed in a single batched solve. For the triaxial tests at lower confining pressures, $p \in \{20, 40, 60, 80\} \text{ kPa}$, the unobserved initial elastic strain and internal variables are treated as auxiliary learnable parameters, while the initial density and macroscopic stress are prescribed from the reference data. These initial states are optimised together with the network weights by enforcing the initial stress residual in Eq. (31). Trajectories are integrated independently under their own loading conditions, but are coupled in the loss through a penalty enforcing state continuity between the connected isotropic and triaxial protocols.

The number of internal variables is selected by training models with $n_\alpha = 0, 1, 2$ and comparing the resulting losses, see Figure 14. The model without internal variables reaches a minimum loss of approximately $6.7 \cdot 10^{-3}$, indicating that density and elastic strain alone are insufficient to represent the observed response. Introducing one scalar internal variable reduces the loss by about a factor of four, while a second one provides only a marginal additional improvement. Following the parsimony criterion of Section 3.3.3, the subsequent results are obtained with $n_\alpha = 1$.

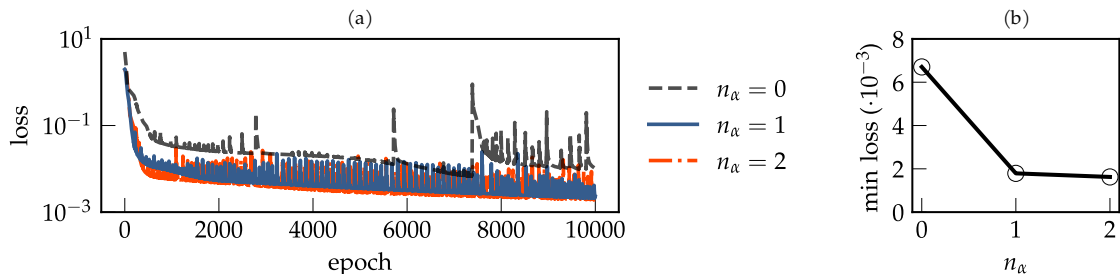


Figure 14: Selection of the number of internal variables. (a) Training loss versus epochs for $n_\alpha = 0, 1, 2$. (b) Minimum training loss as a function of n_α .

5.3 Results

All results presented hereafter are ensemble averages over five independent microstructural realisations generated as described in Section 5.1. Shaded regions indicate the corresponding ensemble spread where light grey bands refer to the numerical simulations and dark grey bands to the predictions of the learned constitutive model.

5.3.1 Predictions on observed loading paths

Figures 15 and 16 show the response under monotonic drained triaxial compression tests, included in the training dataset, starting from $p_0 = 100 \text{ kPa}$ and $p_0 = 20 \text{ kPa}$, respectively. The different columns correspond to simulated granular packings obtained with different compaction friction coefficients μ_c , and hence with different initial densities and microstructural states. The first three rows of Figures 15 and 16 compare the observable macroscopic quantities from the numerical experiments with the learned-model predictions. The neural constitutive model reproduces the main density-dependent trends across the observed densities. Dense packings, obtained for smaller μ_c , exhibit a higher peak stress ratio q/p followed by softening, whereas looser packings show a lower peak and a smoother approach to the q/p plateau. The agreement in the (q, p) plane further indicates that the learned state law recovers the coupling between deviatoric and mean stress during drained triaxial loading. Note that the predictions are obtained by reproducing the control conditions of the corresponding in silico tests. The volumetric response follows from the enforcement of the drained boundary conditions. The model captures the transition from initial compaction to subsequent dilation and its dependence on density. The agreement is particularly clear for dense and intermediate packings. For looser states, the predicted mean response remains close to the reference trend, although a small drift appears at larger strains.

The last two rows display the latent quantities predicted by the model, i.e., the plastic strain and the internal variable. The plastic strain paths $(\varepsilon_v^p, \varepsilon_s^p)$ display a smooth and qualitatively structured evolution, indicating that the learned decomposition is mechanically coherent. The internal variable α also evolves systematically: it remains nearly constant

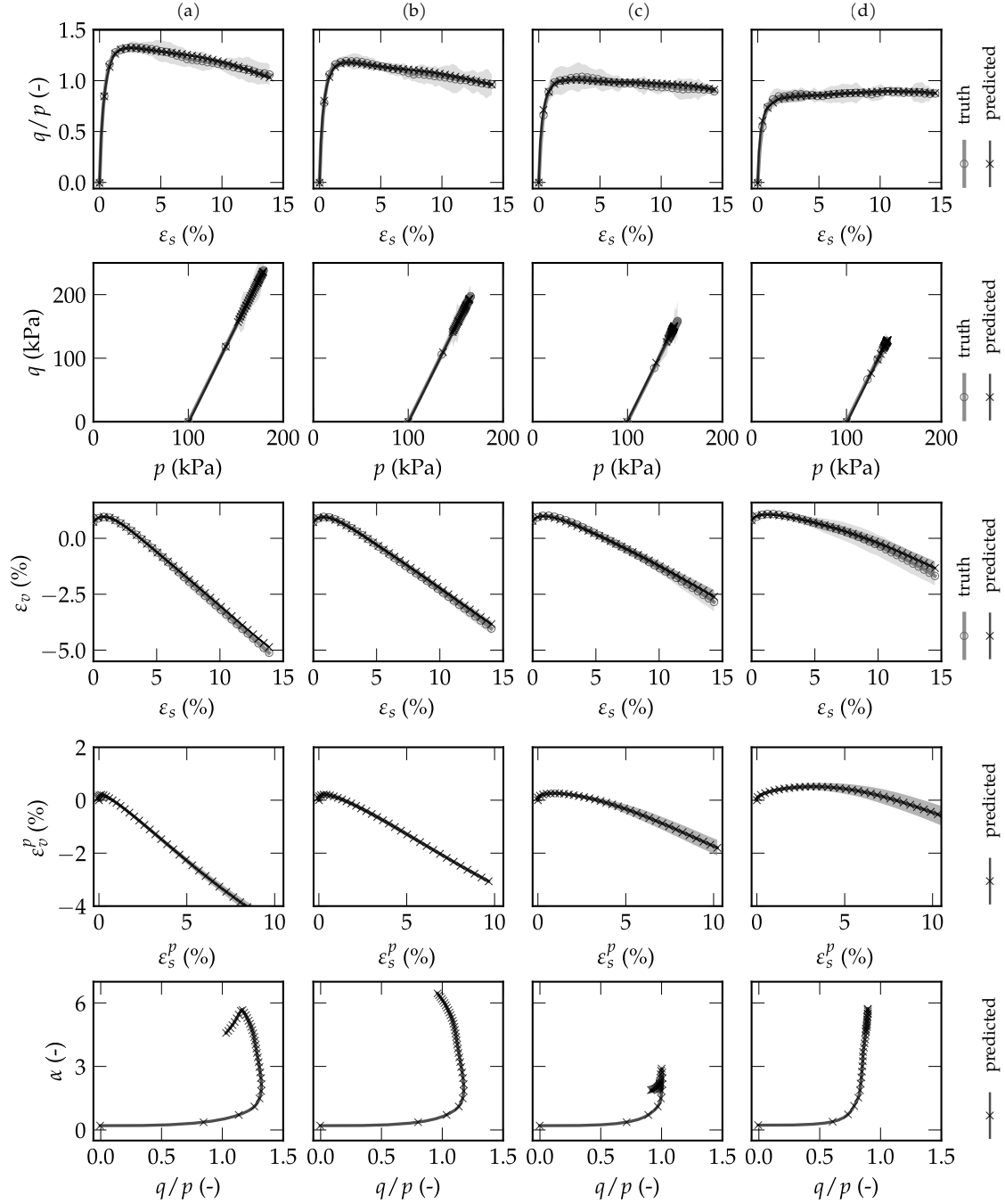


Figure 15: Training predictions for monotonic drained triaxial compression tests at $p_0 = 100$ kPa. Panels correspond to different compaction friction coefficients: (a) $\mu_c = 0$ and $\rho_0/\rho_s = 0.676$, (b) $\mu_c = 0.05$ and $\rho_0/\rho_s = 0.657$, (c) $\mu_c = 0.15$ and $\rho_0/\rho_s = 0.640$, (d) $\mu_c = 0.3$ and $\rho_0/\rho_s = 0.624$. From top to bottom, the rows show the stress ratio q/p versus shear strain ε_s , the deviatoric stress q versus mean pressure p , the volumetric strain ε_v versus ε_s , the plastic volumetric strain ε_v^p versus ε_s^p , and the internal state variable α versus q/p .

during the early stages of loading and changes more rapidly as the stress ratio approaches its peak and subsequent plateau. Overall, the predictions on observed loading paths show that the neural model can fit the reference material responses across different densities and confining pressures.

5.3.2 Generalisation to unseen loading paths

Here, the generalisation capability of the learned model is evaluated considering new, unseen loading paths and protocols.

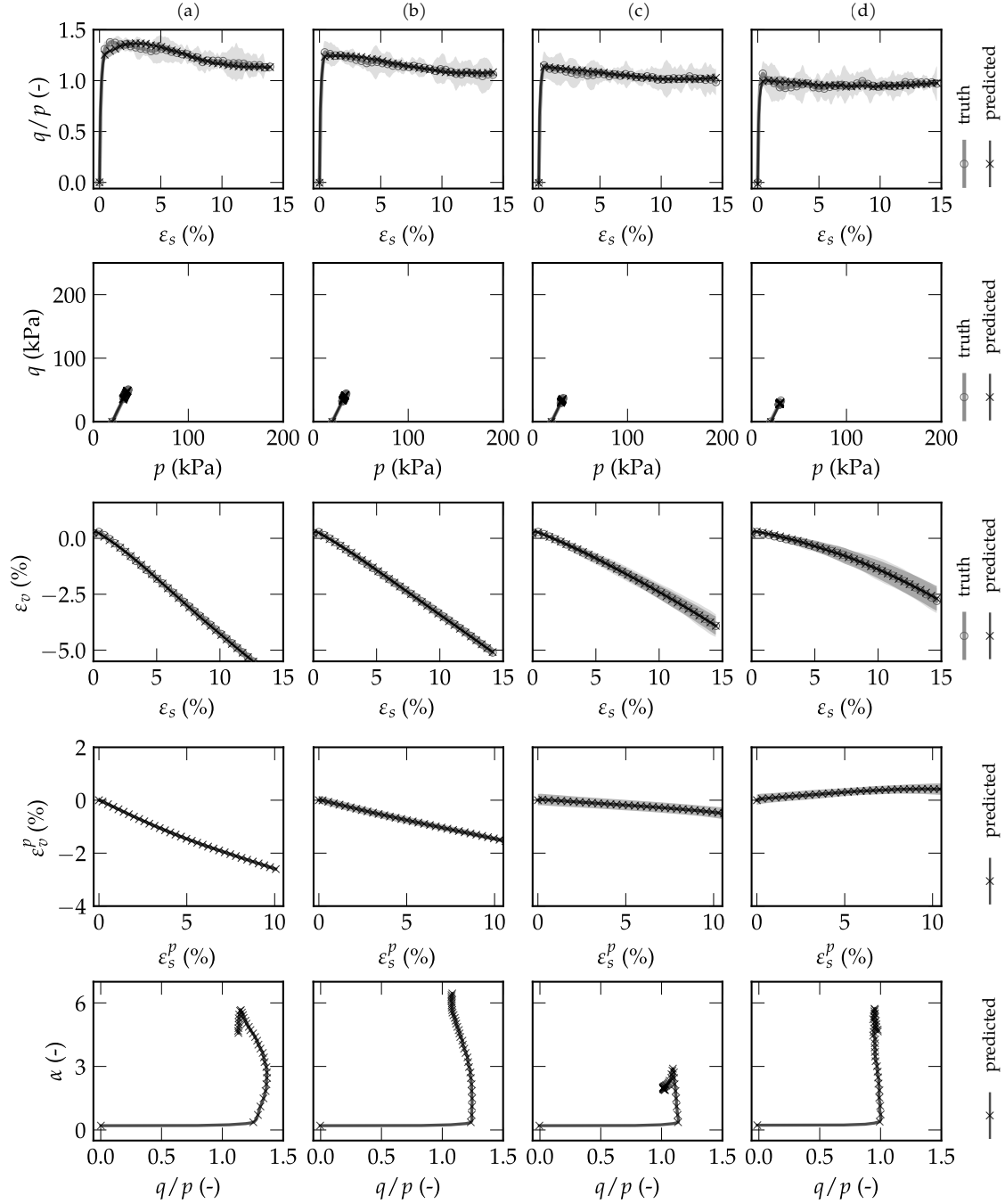


Figure 16: Training predictions for monotonic drained triaxial compression tests at $p_0 = 20$ kPa. Panels correspond to different compaction friction coefficients: (a) $\mu_c = 0$, (b) $\mu_c = 0.05$, (c) $\mu_c = 0.15$, (d) $\mu_c = 0.3$. From top to bottom, the rows show the stress ratio q/p versus shear strain ε_s , the deviatoric stress q versus mean pressure p , the volumetric strain ε_v versus ε_s , the plastic volumetric strain ε_v^p versus ε_s^p , and the internal state variable α versus q/p .

Figure 17 shows drained triaxial compression tests with three loading–unloading sequences at $p_0 = 100$ kPa and different compaction friction coefficients μ_c . The model predicts the unloading–reloading branches with good accuracy, despite having never observed reloading during training. The predicted q/p – ε_s branches reproduce the material response during unloading and reloading, including the changes in stiffness induced by strain reversals, and the (q, p) paths remain close to the numerical experiments throughout the loading sequence. The total volumetric response is also captured well, with the model predicting the accumulated volumetric dilation and the shifts induced by successive reversals. Local discrepancies are mainly visible near reversal points.

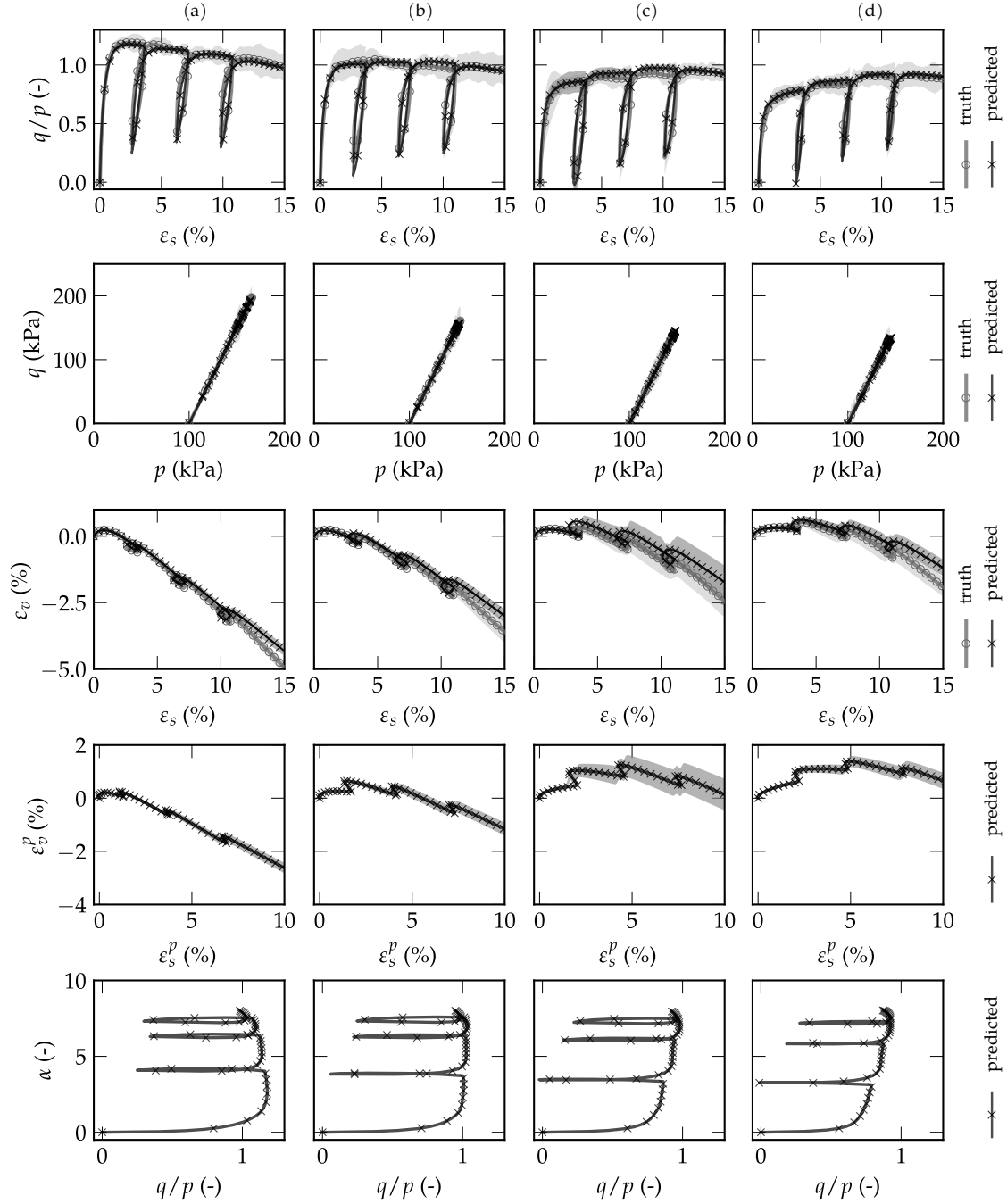


Figure 17: Inference predictions for unobserved drained triaxial compression tests with three loading–unloading sequences at $p_0 = 100$ kPa. Panels correspond to different interparticle preparation friction coefficients: (a) $\mu_c = 0.05$, (b) $\mu_c = 0.15$, (c) $\mu_c = 0.3$, (d) $\mu_c = 0.5$, i.e., $\rho_0/\rho_s = 0.616$. From top to bottom, the rows show the stress ratio q/p versus shear strain ε_s , the deviatoric stress q versus mean pressure p , the volumetric response ε_v versus ε_s , the plastic volumetric strain ε_v^p versus ε_s^p , and the internal variable α versus q/p .

The predicted plastic strain ($\varepsilon_v^p, \varepsilon_s^p$) paths develop distinct branches during loading and unloading, while α follows separated trajectories as the stress ratio is reversed and reloaded. This behaviour suggests that α provides the model with a scalar memory variable needed to distinguish loading from unloading and reloading.

It is worth noting that Figure 17 (d) considers a looser packing ($\mu_c = 0.5$) than those used in training, for which $\mu_c \leq 0.3$. Nevertheless, the model still captures the main stress-ratio and volumetric trends, demonstrating that the learned dependence on density and state variables provides a meaningful extrapolation beyond the observed compaction conditions.

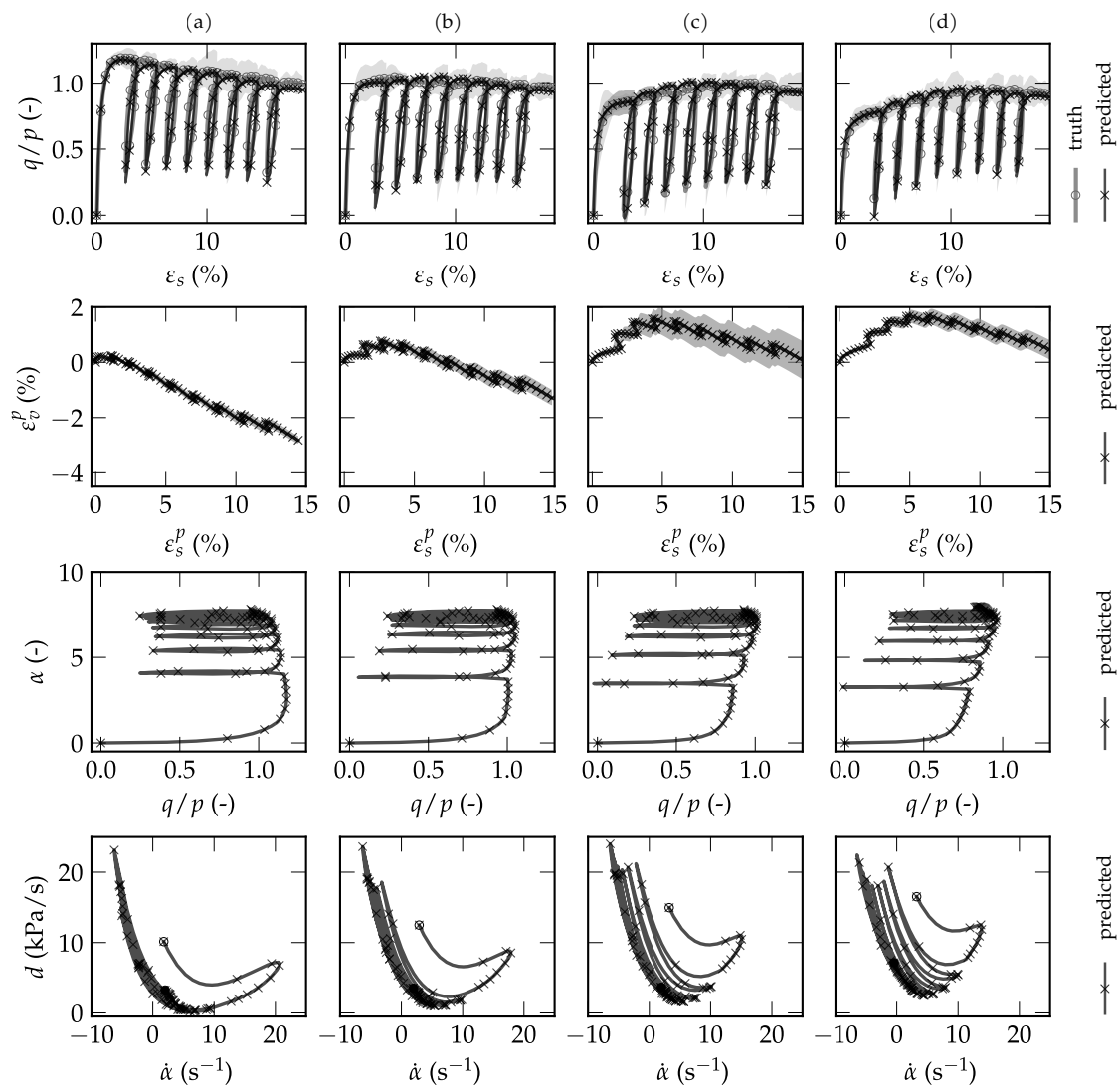


Figure 18: Inference predictions for unobserved drained triaxial compression tests with eight loading–unloading sequences at $p_0 = 100$ kPa. Panels correspond to different interparticle preparation friction coefficients: (a) $\mu_c = 0.05$, (b) $\mu_c = 0.15$, (c) $\mu_c = 0.3$, (d) $\mu_c = 0.5$. From top to bottom, the rows show the stress ratio q/p versus shear strain ε_s , the plastic volumetric strain ε_v^p versus ε_s^p , the internal variable α versus q/p , and the dissipation rate d versus the internal-variable rate $\dot{\alpha}$. Open circles mark the initial value of the d – $\dot{\alpha}$ trajectory, while filled circles mark its final value.

Figure 18 considers the same initial configurations as Figure 17, but increases the number of unloading–reloading sequences from three to eight, with smaller strain amplitudes. The stress-ratio response remains stable over these repeated cycles, and the predicted branches follow the main path-dependent trends of the in silico experiments. Moreover, the model does not accumulate spurious drift or lose stability, despite not having been trained on reloading or cyclic paths and long time horizons.

The latent variables in Figure 18 reveal how the model organises the repeated unloading–reloading sequence. The internal variable α increases during the first loading stages and then evolves within a bounded range, approaching an asymptotic state rather than growing indefinitely. This suggests that α encodes the progressive rearrangement of the granular state until a nearly recurrent cyclic response is reached. Consistently, the trajectories in the d – $\dot{\alpha}$ plane remain non-negative and form cycle-by-cycle loops that drift during the transient stages before approaching a more stable recurrent pattern.

Figure 19 presents unloading–reloading cycles in drained triaxial compression. The three columns correspond to protocols with an increasing number of repeated cycles: (a) one unloading–reloading cycle, (b) two cycles, and (c) three

cycles. These protocols produce clear hysteretic loops in the q/p - ε_s plane, which are accurately reproduced by the model.

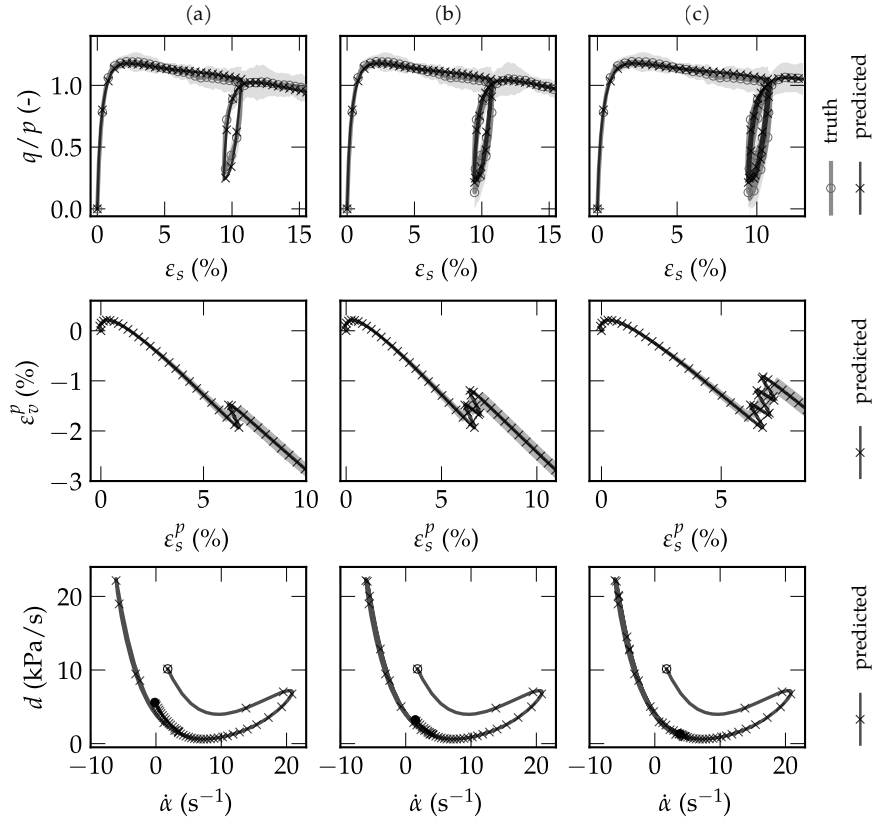


Figure 19: Inference predictions for unobserved cyclic drained triaxial compression tests at $p_0 = 100$ kPa and $\mu_c = 0.05$. Panels correspond to protocols with an increasing number of repeated cycles: (a) one unloading–reloading cycle, (b) two cycles, and (c) three cycles. From top to bottom, the rows show the stress ratio q/p versus shear strain ε_s , the plastic volumetric strain ε_v^p versus ε_s^p , and the dissipation rate d versus the internal-variable rate $\dot{\alpha}$. Open circles mark the initial value of the d - $\dot{\alpha}$ trajectory, while filled circles mark its final value.

The neural model recovers the initial loading branch, the unloading and reloading paths, and the progressive formation of closed loops as the number of cycles increases, with only a slight underestimation of the gradual reduction of q/p , before reversal. The same behaviour is reflected in the inferred plastic strain trajectories.

The dissipation-rate plots provide a thermodynamic view of the same cyclic evolution. The predicted trajectories in the d - $\dot{\alpha}$ plane organise into closed limit cycles, during the repeated cycles. This result is particularly significant because neither plastic strains nor dissipation rates are directly supervised during training, yet they carry qualitative information about the nonlinear hysteretic behaviour of the material.

Finally, Figure 20 considers a loading protocol absent from the training dataset: simple shear with unloading, in which ε_{12} is prescribed while the normal stress components are kept fixed, i.e. $\dot{\sigma}_{11} = \dot{\sigma}_{22} = \dot{\sigma}_{33} = 0$. This mixed-control condition is enforced through the algebraic stress constraints of the constitutive update.

Despite being trained only on isotropic and triaxial paths, the model accurately reproduces the stress-ratio response during shear loading and, to a certain extent, during unloading, with some discrepancies as the unloading progresses.

The model also captures the overall volumetric trend in the $(\varepsilon_v, \varepsilon_s)$ response, but overestimates the contraction after reversal. This limitation is expected, since simple shear probes a loading mode fundamentally outside the training distribution and suggests that a wider class of protocols is required to improve extrapolation under non-triaxial conditions.

Taken together, Figures 17–20 show that the identified constitutive equations generalise beyond the observed monotonic and unloading paths, recovering reloading, hysteretic cycles, and different loading protocols. Particularly interesting is the evolution of the automatically identified internal variable α , which provides a compact latent coordinate through which the model represents material path dependence, while remaining microstructure-agnostic.

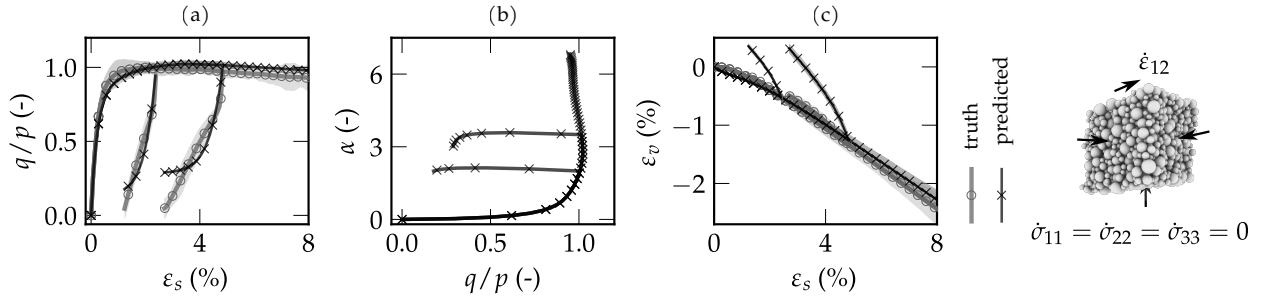


Figure 20: Inference predictions for an unobserved simple-shear test with unloading at $p_0 = 100$ kPa and $\mu_c = 0.15$. From left to right: (a) stress ratio q/p versus shear strain ε_s , (b) internal variable α versus q/p , and (c) volumetric strain ε_v versus shear strain ε_s .

6 Conclusions

This study develops a new pathway to learn and discover constitutive models for complex, inelastic materials grounded in non-equilibrium thermodynamics [18] and, in particular, in the framework of generalised transport equations [30, 79]. The constitutive closure is built on two coupled neural parametrisations: a free-energy density [54, 57] and a state-dependent transport operator that governs the evolution of an autonomously identified material state space. Here, the first law of thermodynamics is enforced through an energetic parametrisation of the state laws, and the second law is satisfied exactly by restricting the symmetric part of the transport operator to be positive semidefinite [79], while retaining skew-symmetric couplings to represent reversible interactions and mixed reversible–irreversible effects. The framework additionally hardwires frame indifference and thermodynamic stability via invariant representations and a convex free-energy ansatz, while automatically identifying a stress-free reference equilibrium state. Unlike soft-constraint approaches that may drift into thermodynamic violations when trained on limited datasets (cf. [52]), and unlike many hard-constrained formulations that rely on restrictive templates (e.g. dissipation pseudo-potentials [18, 31, 59]), this pathway defines an admissible yet flexible hypothesis class able to represent complex materials, including non-associative and path-dependent behaviours, from stress–strain data alone. The framework also removes the need to access state variables, such as elastic (or plastic) strain and internal variables, that are not directly measurable from conventional laboratory experiments without additional modelling assumptions.

The performance of the framework was validated on synthetic benchmarks generated from analytical material models of increasing complexity, spanning elasto- and hypo-plasticity, rate effects, hardening, and a non-associative plasticity. Across these cases, the automatically identified models reproduce the observed stress histories with high accuracy while simultaneously delivering internally consistent thermodynamic variables (free energy, dissipation rate, and state evolution) despite these quantities not being observed at training time. The benchmarks also illustrate that the method can recover interpretable internal variables when they are necessary to represent the data (e.g., a hardening-like variable emerging without supervision), and can generalise to qualitatively different and more demanding loading paths under mixed control. In the non-associative benchmark, the framework extrapolates from triaxial data to constant-pressure shear while correctly capturing the inherent non-associative flow rule, highlighting that the general transport structure can represent non-associative mechanisms without relying on a dissipation potential while preserving thermodynamic admissibility.

The framework was further applied to granular materials using discrete-element *in silico* experiments, restricting the training data to macroscopic stress–strain histories and initial density so that grain-scale descriptors remain unobserved. The discovered constitutive model reproduces monotonic and non-monotonic responses and extrapolates to unseen cyclic loading paths and different protocols, including hysteresis absent from the training data.

While the presented framework relies on a Cauchy continuum description, restricted to isothermal processes, the general non-equilibrium thermodynamic setting it builds upon can be naturally extended to generalised continua [29, 38, 58, 67], i.e., nonlocal and high-order formulations, by simply expanding the stress–strain space. In this context, the dual internal variable theory [5, 79], which proposes a unifying description of internal variables and internal degrees of freedom, offers a compelling standpoint to enrich the state space without relying on ad hoc closures (cf. [66]).

It is worth mentioning that the proposed framework is general and can be applied to a wide range of materials with complex microstructural effects. In this work, the results demonstrated that accurate macroscopic laws can be discovered in a microstructure-agnostic setting, even when only conventional stress–strain histories are available. Yet, whenever microstructural observations are accessible, the same approach can be coupled to automatically discovered descriptors of the evolving microstructure to promote identifiability of the discovered internal state variables (see [54, 55]).

Application of the present methodology to real experimental observations is a natural next step. In that setting, the hard-constrained structure is expected to act both as a robustness mechanism under noisy and sparse measurements and as an explicit diagnostic of thermodynamic admissibility under extrapolation.

Supplementary material

The implementations of the thermodynamics-constrained constitutive learning framework, together with the codes for the benchmarks and applications, will be made available at <https://github.com/hard-constitutive-learning>.

Acknowledgements

I would like to thank Prof. Itai Einav for insightful discussions on the theoretical foundations of the Onsager-Casimir reciprocity relations, and Dr. Vincent Acary for valuable exchanges on the implementation of the proposed methodology. This work was supported by the Multidisciplinary Institute in Artificial Intelligence (MIAI) Cluster and the *Agence Nationale de la Recherche* through the France 2030 program (Grant agreement ANR-23-IACL-0006) within the chair AIM: Artificial Intelligence and Mechanics for scale bridging in complex materials.

Declaration of competing interests

The author declares no competing interests.

Declaration of generative AI and AI-assisted technologies

During the preparation of this manuscript, the author used OpenAI's large language model, ChatGPT, to assist with text refinement and grammar checking. After using this tool, the author reviewed and edited the content as needed and takes full responsibility for the content of the present manuscript.

A Classification based on the total strain

One may prefer not to assume the existence of elastic strain, to any extent, when setting a general classification for the material state space. Here, we present the derivation of Section 2 with a state space specified as $\mathbf{s} = (\rho, \boldsymbol{\varepsilon}, \boldsymbol{\alpha})$, where we use the total strain as state variable. Consequently, the free energy density and the energetic stress are specified as

$$\psi \equiv \psi(\rho, \boldsymbol{\varepsilon}, \boldsymbol{\alpha}), \quad \boldsymbol{\sigma}^e \equiv \rho \frac{\partial \psi}{\partial \boldsymbol{\varepsilon}}(\rho, \boldsymbol{\varepsilon}, \boldsymbol{\alpha}), \quad (\text{A.1})$$

while the chemical potential and energetic forces associated with the internal variables are defined in Eq. (9). Following the same procedure presented in Section 2, the dissipation inequality reads

$$d = \mathcal{A}^d \circ \dot{\boldsymbol{\alpha}} + \boldsymbol{\sigma}^d : \dot{\boldsymbol{\varepsilon}} = \boldsymbol{\mathcal{Y}} \circ \mathbf{z} \geq 0, \quad \boldsymbol{\mathcal{Y}} \equiv (\mathcal{A}^d \quad \boldsymbol{\sigma}^d), \quad \mathbf{z} \equiv (\dot{\boldsymbol{\alpha}} \quad \dot{\boldsymbol{\varepsilon}}), \quad (\text{A.2})$$

where $\boldsymbol{\sigma}^d \equiv \boldsymbol{\sigma} - [\boldsymbol{\sigma}^e - \rho \mu \mathbf{I}]$ and $\mathcal{A}^d \equiv -\rho \partial \psi / \partial \boldsymbol{\alpha}$. A general solution to the dissipation inequality is thus given by $\mathbf{z} = \mathbb{L} \boldsymbol{\mathcal{Y}}$, i.e.,

$$\begin{pmatrix} \dot{\boldsymbol{\alpha}} \\ \dot{\boldsymbol{\varepsilon}} \end{pmatrix} = \begin{pmatrix} \mathbf{L}^{11} & \mathbf{L}^{12} \\ \mathbf{L}^{21} & \mathbf{L}^{22} \end{pmatrix} \begin{pmatrix} \mathcal{A}^d \\ \boldsymbol{\sigma}^d \end{pmatrix}. \quad (\text{A.3})$$

with $\text{Sym}(\mathbb{L}) \succeq 0$.

B Hard versus soft enforcement of the dissipation inequality

The impact of enforcing the dissipation inequality by construction (hard constraint) versus enforcing it through a penalty term (soft constraint) is assessed on the one-dimensional elasto-plastic benchmark with isotropic hardening (Section 4.1.4). For completeness, two penalty-based alternatives for the evolution law are considered, namely

- soft-direct: a direct evolution network (cf. [52]), i.e., $\mathbf{z} = \mathbf{g}_\theta(\mathbf{s}, \boldsymbol{\mathcal{Y}})$ and
- soft-transport: a transport relation $\mathbf{z} = \mathbb{L}_\theta(\mathbf{s}, \boldsymbol{\mathcal{Y}}) \boldsymbol{\mathcal{Y}}$ where the symmetric part of \mathbb{L}_θ is not constrained to be positive semidefinite.

In both cases, the objective in Eq. (32) is augmented with a penalty loss term on negative dissipation,

$$\boldsymbol{\theta}^* = \arg \min_{\boldsymbol{\theta}} \frac{1}{n_P} \sum_{p=1}^{n_P} \left[\frac{1}{n_T} \sum_{k=1}^{n_T} \left\| \boldsymbol{\sigma}(s_k^{(p)}; \boldsymbol{\theta}) - \bar{\boldsymbol{\sigma}}_k^{(p)} \right\|_2^2 + \left\| \mathcal{R}(s_0^{(p)}, \bar{\boldsymbol{\sigma}}_0^{(p)}; \boldsymbol{\theta}) \right\|_2^2 + \frac{1}{n_T} \sum_{k=1}^{n_T} \left[\max(0, -d(s_k^{(p)}; \boldsymbol{\theta})) \right]^2 \right], \quad (\text{B.1})$$

where $d(s; \boldsymbol{\theta})$ denotes the dissipation rate computed from the inner product between the predicted thermodynamic forces and fluxes.

All comparisons use the same free-energy architecture, state-law parametrisations, training protocols, optimiser settings, numerical integration scheme, initialisation, and random seeds, as well as the same number of trainable parameters for the evolution model, see Section 4.1.4. Training is performed for 4000 epochs for all three variants.

Figure B.21 compares the three formulations (hard-constrained, soft-direct, and soft-transport) for one of the training loading protocols. All formulations achieve comparable stress–strain fits on the training data, indicating that the observed stress response alone does not strongly discriminate between enforcement strategies for the dissipation inequality or between the chosen evolution parametrisations.

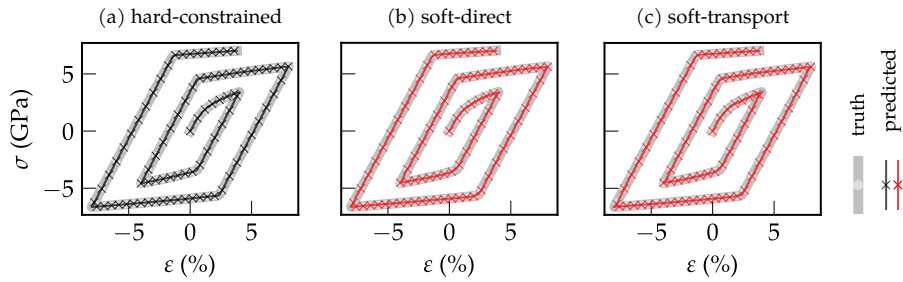


Figure B.21: Stress–strain response for one training loading protocol: (a) hard-constrained formulation, (b–c) soft-constrained variants. All formulations achieve comparable fits on the training data.

Generalisation is then assessed on the unseen cyclic loading protocol presented in Figure 6. Figure B.22 compares predictions with the ground truth. Although the soft-constraint variants exhibit non-negative dissipation rates for this protocol, they yield degraded performances in extrapolation in terms of (i) the stress hysteresis, (ii) the functional dependence of the dissipation rate $d(\dot{\epsilon}^P)$, and (iii) the evolution of the learned internal variable. This indicates that penalising violations of $d \geq 0$ during training can be insufficient to constrain the learned evolution operator outside the training distribution: multiple evolution laws can fit the training data while remaining weakly constrained and may fail to generalise. In contrast, the hard-constrained formulation provides more reliable extrapolation and more consistently recovers the hidden state variable.

References

- [1] E. Alaei, B. Marks, and I. Einav. A hydrodynamic-plastic formulation for modelling sand using a minimal set of parameters. *Journal of the Mechanics and Physics of Solids*, 151:104388, 2021. doi: <https://doi.org/10.1016/j.jmps.2021.104388>.
- [2] B. Amos, L. Xu, and J. Z. Kolter. Input convex neural networks. In D. Precup and Y. W. Teh, editors, *Proceedings of the 34th International Conference on Machine Learning*, volume 70 of *Proceedings of Machine Learning Research*, pages 146–155. PMLR, 06–11 Aug 2017.
- [3] F. As’ad and C. Farhat. A mechanics-informed deep learning framework for data-driven nonlinear viscoelasticity. *Computer Methods in Applied Mechanics and Engineering*, 417:116463, 2023. doi: <https://doi.org/10.1016/j.cma.2023.116463>.
- [4] J. M. Ball. Convexity conditions and existence theorems in nonlinear elasticity. *Archive for rational mechanics and Analysis*, 63:337–403, 1976. doi: <https://doi.org/10.1007/BF00279992>.
- [5] A. Berezovski. Internal variables associated with microstructures in solids. *Mechanics Research Communications*, 93:30–34, 2018. doi: <https://doi.org/10.1016/j.mechrescom.2017.07.011>.

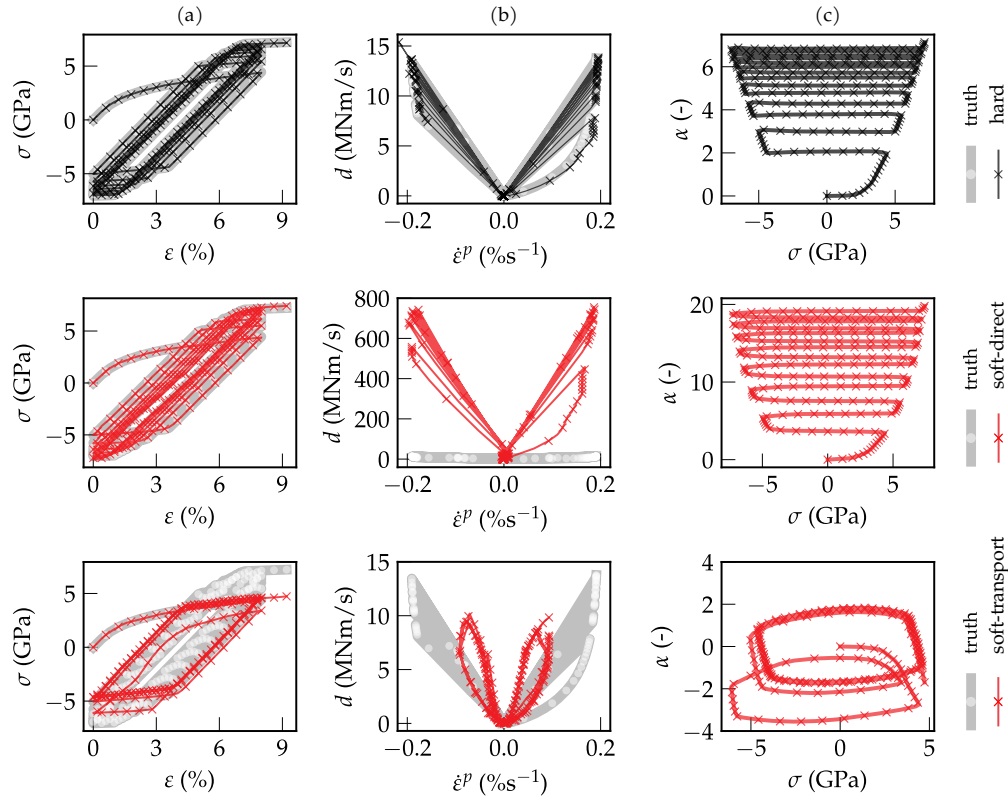


Figure B.22: Predictions on the unseen cyclic loading protocol of Fig. 6 for the hard-constrained (top) and soft-constrained implementations, S1 (middle) and S2 (bottom). From left to right: (a) stress versus strain (σ - ε), (b) dissipation rate versus plastic strain rate (d - $\dot{\varepsilon}^p$), (c) automatically identified internal variable α . Panel (b) uses different vertical axis limits across rows to accommodate the larger dissipation magnitudes of the soft-S1 variant.

- [6] A. Berezovski and P. Ván. Microinertia and internal variables. *Continuum Mechanics and Thermodynamics*, 28(4): 1027–1037, 2016. doi: <https://doi.org/10.1007/s00161-015-0453-2>.
- [7] J. Bleyer. Learning elastoplasticity with implicit layers. *Computer Methods in Applied Mechanics and Engineering*, 444:118145, 2025. doi: <https://doi.org/10.1016/j.cma.2025.118145>.
- [8] C. Bonatti and D. Mohr. On the importance of self-consistency in recurrent neural network models representing elasto-plastic solids. *Journal of the Mechanics and Physics of Solids*, 158:104697, 2022. doi: <https://doi.org/10.1016/j.jmps.2021.104697>.
- [9] H. B. G. Casimir. On Onsager’s Principle of Microscopic Reversibility. *Reviews of Modern Physics*, 17:343–350, 1945. doi: <https://doi.org/10.1103/RevModPhys.17.343>.
- [10] P. Chen and J. Guilleminot. Polyconvex neural networks for hyperelastic constitutive models: A rectification approach. *Mechanics Research Communications*, 125:103993, 2022. doi: <https://doi.org/10.1016/j.mechrescom.2022.103993>.
- [11] R. T. Chen, Y. Rubanova, J. Bettencourt, and D. K. Duvenaud. Neural ordinary differential equations. *Advances in neural information processing systems*, 31, 2018.
- [12] R. T. Q. Chen. TorchDiffEq, 2018. URL <https://github.com/rtqichen/torchdiffeq>.
- [13] B. D. Coleman and M. E. Gurtin. Thermodynamics with internal state variables. *The Journal of Chemical Physics*, 47(2):597–613, 1967. doi: <https://doi.org/10.1063/1.1711937>.
- [14] O. Coussy. *Mechanics and physics of porous solids*. John Wiley & Sons, 2010. doi: <https://doi.org/10.1002/9780470710388>.
- [15] E. Cueto and F. Chinesta. Thermodynamics of learning physical phenomena. *Archives of Computational Methods in Engineering*, 30(8):4653–4666, 2023. doi: <https://doi.org/10.1007/s11831-023-09954-5>.

- [16] P. A. Cundall and O. D. Strack. A discrete numerical model for granular assemblies. *Géotechnique*, 29(1):47–65, 1979. doi: <https://doi.org/10.1680/geot.1979.29.1.47>.
- [17] W. M. Czarnecki, S. Osindero, M. Jaderberg, G. Swirszcz, and R. Pascanu. Sobolev training for neural networks. *Advances in neural information processing systems*, 30, 2017.
- [18] S. R. De Groot and P. Mazur. *Non-equilibrium thermodynamics*. Dover Publications, 2013.
- [19] G. de Saxcé and L. Bousshine. *Implicit Standard Materials*, pages 59–76. Springer Vienna, Vienna, 2002. ISBN 978-3-7091-2558-8. doi: https://doi.org/10.1007/978-3-7091-2558-8_4.
- [20] G. de Saxcé and Z.-Q. Feng. New inequality and functional for contact with friction: the implicit standard material approach. *Journal of Structural Mechanics*, 19(3):301–325, 1991. doi: <https://doi.org/10.1080/08905459108905146>.
- [21] I. Einav. The unification of hypo-plastic and elasto-plastic theories. *International Journal of Solids and Structures*, 49(11-12):1305–1315, 2012. doi: <https://doi.org/10.1016/j.ijsolstr.2012.02.003>.
- [22] I. Einav and M. Liu. Hydrodynamic derivation of the work input to fully and partially saturated soils. *Journal of the Mechanics and Physics of Solids*, 110:205–217, 2018. doi: <https://doi.org/10.1016/j.jmps.2017.10.004>.
- [23] I. Einav and M. Liu. Hydrodynamics of non-equilibrium soil water retention. *Water Resources Research*, 59(1): e2022WR033409, 2023. doi: <https://doi.org/10.1029/2022WR033409>.
- [24] M. Flaschel, S. Kumar, and L. De Lorenzis. Automated discovery of generalized standard material models with EUCLID. *Computer Methods in Applied Mechanics and Engineering*, 405:115867, 2023. doi: <https://doi.org/10.1016/j.cma.2022.115867>.
- [25] M. Flaschel, P. Steinmann, L. De Lorenzis, and E. Kuhl. Convex neural networks learn generalized standard material models. *Journal of the Mechanics and Physics of Solids*, 200:106103, 2025. doi: <https://doi.org/10.1016/j.jmps.2025.106103>.
- [26] J. N. Fuhg, G. A. Padmanabha, N. Bouklas, B. Bahmani, W. Sun, N. N. Vlassis, M. Flaschel, P. Carrara, and L. De Lorenzis. A review on data-driven constitutive laws for solids. *Archives of Computational Methods in Engineering*, 32:1841–1883, 2025. doi: <https://doi.org/10.1007/s11831-024-10196-2>.
- [27] GDR MiDi. On dense granular flows. *The European Physical Journal E*, 14:341–365, 2004. doi: <https://doi.org/10.1140/epje/i2003-10153-0>.
- [28] M. G. Geers, V. G. Kouznetsova, and W. Brekelmans. Multi-scale computational homogenization: Trends and challenges. *Journal of computational and applied mathematics*, 234(7):2175–2182, 2010. doi: <https://doi.org/10.1016/j.cam.2009.08.077>.
- [29] P. Germain. The method of virtual power in continuum mechanics. Part 2: Microstructure. *SIAM Journal on Applied Mathematics*, 25(3):556–575, 1973. doi: <https://doi.org/10.1137/0125053>.
- [30] M. E. Gurtin. Generalized Ginzburg-Landau and Cahn-Hilliard equations based on a microforce balance. *Physica D: Nonlinear Phenomena*, 92(3-4):178–192, 1996. doi: [https://doi.org/10.1016/0167-2789\(95\)00173-5](https://doi.org/10.1016/0167-2789(95)00173-5).
- [31] B. Halphen and Q. S. Nguyen. Sur les matériaux standard généralisés. *Journal de mécanique*, 14(1):39–63, 1975.
- [32] Y. Heider, K. Wang, and W. Sun. SO(3)-invariance of informed-graph-based deep neural network for anisotropic elastoplastic materials. *Computer Methods in Applied Mechanics and Engineering*, 363:112875, 2020. doi: [10.1016/j.cma.2020.112875](https://doi.org/10.1016/j.cma.2020.112875).
- [33] Q. Hernandez, A. Badias, D. Gonzalez, F. Chinesta, and E. Cueto. Deep learning of thermodynamics-aware reduced-order models from data. *Computer Methods in Applied Mechanics and Engineering*, 379:113763, 2021. doi: <https://doi.org/10.1016/j.cma.2021.113763>.
- [34] H. Holthusen, L. Lamm, T. Brepols, S. Reese, and E. Kuhl. Theory and implementation of inelastic constitutive artificial neural networks. *Computer Methods in Applied Mechanics and Engineering*, 428:117063, 2024. doi: <https://doi.org/10.1016/j.cma.2024.117063>.

- [35] H. Holthusen, K. Linka, E. Kuhl, and T. Brepols. A generalized dual potential for inelastic constitutive artificial neural networks: A JAX implementation at finite strains. *Journal of the Mechanics and Physics of Solids*, 206:106337, 2025. doi: <https://doi.org/10.1016/j.jmps.2025.106337>.
- [36] G. T. Houlsby and A. M. Puzrin. *Principles of Hyperplasticity*. Springer London, 2007. doi: <https://doi.org/10.1007/978-1-84628-240-9>.
- [37] S. Huang, Z. He, and C. Reina. Variational Onsager Neural Networks (VONNs): A thermodynamics-based variational learning strategy for non-equilibrium PDEs. *Journal of the Mechanics and Physics of Solids*, 163:104856, 2022. doi: <https://doi.org/10.1016/j.jmps.2022.104856>.
- [38] P. Ireman and Q.-S. Nguyen. Using the gradients of temperature and internal parameters in continuum thermodynamics. *Comptes Rendus Mécanique*, 332(4):249–255, 2004. doi: <https://doi.org/10.1016/j.crme.2004.01.012>.
- [39] C. Jailin and E. Baranger. Material-embedding Physics-Augmented Neural Networks: A first application to constitutive law parameterization. *Computer Methods in Applied Mechanics and Engineering*, 445:118188, 2025. doi: <https://doi.org/10.1016/j.cma.2025.118188>.
- [40] Y. Jiang and M. Liu. Granular solid hydrodynamics. *Granular Matter*, 11:139–156, 2009. doi: <https://doi.org/10.1007/s10035-009-0137-3>.
- [41] Y. Jiang and M. Liu. Applying GSH to a wide range of experiments in granular media. *The European Physical Journal E*, 38:1–27, 2015. doi: <https://doi.org/10.1140/epje/i2015-15015-6>.
- [42] K. Karapiperis, L. Stainier, M. Ortiz, and J. E. Andrade. Data-driven multiscale modeling in mechanics. *Journal of the Mechanics and Physics of Solids*, 147:104239, 2021. doi: <https://doi.org/10.1016/j.jmps.2020.104239>.
- [43] G. E. Karniadakis, I. G. Kevrekidis, L. Lu, P. Perdikaris, S. Wang, and L. Yang. Physics-informed machine learning. *Nature Reviews Physics*, 3(6):422–440, 2021. doi: <https://doi.org/10.1038/s42254-021-00314-5>.
- [44] R. Kawamoto, E. Andò, G. Viggiani, and J. E. Andrade. All you need is shape: Predicting shear banding in sand with LS-DEM. *Journal of the Mechanics and Physics of Solids*, 111:375–392, 2018. doi: <https://doi.org/10.1016/j.jmps.2017.10.003>.
- [45] D. K. Klein, M. Fernández, R. J. Martin, P. Neff, and O. Weeger. Polyconvex anisotropic hyperelasticity with neural networks. *Journal of the Mechanics and Physics of Solids*, 159:104703, 2022. doi: <https://doi.org/10.1016/j.jmps.2021.104703>.
- [46] D. Kolymbas. An outline of hypoplasticity. *Archive of applied mechanics*, 61(3):143–151, 1991. doi: <https://doi.org/10.1007/BF00788048>.
- [47] D. Kolymbas. The misery of constitutive modelling. In *Constitutive modelling of granular materials*, pages 11–24. Springer, 2000. doi: https://doi.org/10.1007/978-3-642-57018-6_1.
- [48] J. Kozicki and F. V. Donze. YADE-OPEN DEM: An open-source software using a discrete element method to simulate granular material. *Engineering Computations*, 26(7):786–805, 2009.
- [49] L. Linden, D. K. Klein, K. A. Kalina, J. Brummund, O. Weeger, and M. Kästner. Neural networks meet hyperelasticity: A guide to enforcing physics. *Journal of the Mechanics and Physics of Solids*, 179:105363, 2023. doi: <https://doi.org/10.1016/j.jmps.2023.105363>.
- [50] K. Linka and E. Kuhl. A new family of constitutive artificial neural networks towards automated model discovery. *Computer Methods in Applied Mechanics and Engineering*, 403:115731, 2023. doi: <https://doi.org/10.1016/j.cma.2022.115731>.
- [51] A. E. H. Love. *A treatise on the mathematical theory of elasticity*. Cambridge University Press, 1892.
- [52] F. Masi and I. Einav. Neural integration for constitutive equations using small data. *Computer Methods in Applied Mechanics and Engineering*, 420:116698, 2024. doi: <https://doi.org/10.1016/j.cma.2023.116698>.
- [53] F. Masi and I. Einav. Hydrodynamics of fault gouges from constitutive modelling to the physics of friction. *Journal of Geophysical Research: Solid Earth*, 130:e2024JB030822, 2025. doi: <https://doi.org/10.1029/2024JB030822>.

- [54] F. Masi and I. Stefanou. Multiscale modeling of inelastic materials with Thermodynamics-based Artificial Neural Networks (TANN). *Computer Methods in Applied Mechanics and Engineering*, 398:115190, 2022. doi: <https://doi.org/10.1016/j.cma.2022.115190>.
- [55] F. Masi and I. Stefanou. Evolution TANN and the identification of internal variables and evolution equations in solid mechanics. *Journal of the Mechanics and Physics of Solids*, 174:105245, 2023. doi: <https://doi.org/10.1016/j.jmps.2023.105245>.
- [56] F. Masi and I. Stefanou. *Physics-Informed and Thermodynamics-Based Neural Networks*, chapter 3, pages 57–100. John Wiley & Sons, Ltd, 2024. ISBN 9781394325665. doi: <https://doi.org/10.1002/9781394325665.ch3>.
- [57] F. Masi, I. Stefanou, P. Vannucci, and V. Maffi-Berthier. Thermodynamics-based artificial neural networks for constitutive modeling. *Journal of the Mechanics and Physics of Solids*, 147:104277, 2021. doi: <https://doi.org/10.1016/j.jmps.2020.104277>.
- [58] G. A. Maugin. Internal variables and dissipative structures. *Journal of Non-Equilibrium Thermodynamics*, 15: 173–192, 1990. doi: <https://doi.org/10.1515/jnet.1990.15.2.173>.
- [59] A. McBride, B. D. Reddy, and P. Steinmann. Dissipation-consistent modelling and classification of extended plasticity formulations. *Journal of the Mechanics and Physics of Solids*, 119:118–139, 2018. doi: <https://doi.org/10.1016/j.jmps.2018.06.002>.
- [60] F. J. Montáns, F. Chinesta, R. Gómez-Bombarelli, and J. N. Kutz. Data-driven modeling and learning in science and engineering. *Comptes Rendus Mécanique*, 347(11):845–855, 2019. doi: <https://doi.org/10.1016/j.crme.2019.11.009>.
- [61] J. J. Moreau. Sur les lois de frottement, de plasticité et de viscosité. *Comptes rendus hebdomadaires des séances de l'Académie des sciences*, 271:608–611, 1970.
- [62] J. J. Moreau. *On Unilateral Constraints, Friction and Plasticity*, pages 171–322. Springer Berlin Heidelberg, Berlin, Heidelberg, 1973. doi: https://doi.org/10.1007/978-3-642-10960-7_7.
- [63] L. Onsager. Reciprocal Relations in Irreversible Processes. I. *Physical Review*, 37:405–426, 1931. doi: <https://doi.org/10.1103/PhysRev.37.405>.
- [64] L. Onsager. Reciprocal Relations in Irreversible Processes. II. *Physical Review*, 38:2265–2279, 1931. doi: <https://doi.org/10.1103/PhysRev.38.2265>.
- [65] C. O’Sullivan. *Particulate discrete element modelling: a geomechanics perspective*. CRC Press, 2011.
- [66] H. C. Öttinger. *Beyond equilibrium thermodynamics*. John Wiley & Sons, 2005. doi: <https://doi.org/10.1002/0471727903>.
- [67] C. Papenfuss and S. Forest. Thermodynamical frameworks for higher grade material theories with internal variables or additional degrees of freedom. *Journal of Non-Equilibrium Thermodynamics*, 2006. doi: <https://doi.org/10.1515/jnetdy.2006.014>.
- [68] A. Paszke, S. Gross, S. Chintala, G. Chanan, E. Yang, Z. DeVito, Z. Lin, A. Desmaison, L. Antiga, and A. Lerer. Automatic differentiation in pytorch. *Neural Information Processing Systems*, 2017.
- [69] W. Qiu, S. Huang, and C. Reina. Bridging statistical mechanics and thermodynamics away from equilibrium: a data-driven approach for learning internal variables and their dynamics. *Journal of the Mechanics and Physics of Solids*, page 106211, 2025. doi: <https://doi.org/10.1016/j.jmps.2025.106211>.
- [70] W. Ramberg and W. R. Osgood. Description of stress-strain curves by three parameters. NACA-TN-902, National Advisory Committee For Aeronautics, Washington DC, 1943.
- [71] M. Rosenkranz, K. A. Kalina, J. Brummund, W. Sun, and M. Kästner. Viscoelasticity with physics-augmented neural networks: model formulation and training methods without prescribed internal variables. *Computational Mechanics*, 74(6):1279–1301, 2024. doi: <https://doi.org/10.1007/s00466-024-02477-1>.
- [72] M. Rubin. Plasticity theory formulated in terms of physically based microstructural variables—Part I. Theory. *International journal of solids and structures*, 31(19):2615–2634, 1994. doi: [https://doi.org/10.1016/0020-7683\(94\)90222-4](https://doi.org/10.1016/0020-7683(94)90222-4).

- [73] A. N. Schofield and P. Wroth. *Critical state soil mechanics*, volume 310. McGraw-hill London, 1968.
- [74] J. Schröder and P. Neff. Construction of polyconvex, anisotropic free-energy functions. In *PAMM: Proceedings in Applied Mathematics and Mechanics*, volume 2, pages 172–173. Wiley Online Library, 2003.
- [75] A. Stathas and I. Stefanou. The role of viscous regularization in dynamical problems, strain localization and mesh dependency. *Computer Methods in Applied Mechanics and Engineering*, 388:114185, 2022. doi: <https://doi.org/10.1016/j.cma.2021.114185>.
- [76] M. Tafili, J. Duque, D. Mašín, and T. Wichtmann. A hypoplastic model for pre-and post-liquefaction analysis of sands. *Computers and Geotechnics*, 171:106314, 2024. doi: <https://doi.org/10.1016/j.compgeo.2024.106314>.
- [77] M. Taiebat and Y. F. Dafalias. SANISAND: Simple anisotropic sand plasticity model. *International Journal for numerical and analytical methods in geomechanics*, 32(8):915–948, 2008. doi: <https://doi.org/10.1002/nag.651>.
- [78] A. Tengattini, E. Andò, I. Einav, and G. Viggiani. Micromechanically inspired investigation of cemented granular materials: part I—from X-ray micro tomography to measurable model variables. *Acta Geotechnica*, 18(1):35–55, 2023. doi: <https://doi.org/10.1007/s11440-022-01486-9>.
- [79] P. Ván, A. Berezovski, and J. Engelbrecht. Internal variables and dynamic degrees of freedom. *Journal of Non-Equilibrium Thermodynamics*, 2008. doi: <https://doi.org/10.1515/jnetdy.2008.010>.
- [80] I. Vlahinić, E. Andò, G. Viggiani, and J. E. Andrade. Towards a more accurate characterization of granular media: extracting quantitative descriptors from tomographic images. *Granular Matter*, 16(1):9–21, 2014. doi: <https://doi.org/10.1007/s10035-013-0460-6>.
- [81] N. N. Vlassis and W. Sun. Sobolev training of thermodynamic-informed neural networks for interpretable elasto-plasticity models with level set hardening. *Computer Methods in Applied Mechanics and Engineering*, 377:113695, 2021. doi: <https://doi.org/10.1016/j.cma.2021.113695>.
- [82] N. N. Vlassis and W. Sun. Geometric learning for computational mechanics Part II: Graph embedding for interpretable multiscale plasticity. *Computer Methods in Applied Mechanics and Engineering*, 404:115768, 2023. doi: <https://doi.org/10.1016/j.cma.2022.115768>.
- [83] J. Weber. Recherches concernant les contraintes intergranulaires dans les milieux pulvérulents. *Bulletin de Liaison des Ponts-et-chaussées*, 20:1–20, 1966.
- [84] M. Wiebicke and I. Einav. A simple hydrodynamic model for clay. *Journal of the Mechanics and Physics of Solids*, page 105789, 2024. doi: <https://doi.org/10.1016/j.jmps.2024.105789>.
- [85] H. Ziegler. An attempt to generalize Onsager’s principle, and its significance for rheological problems. *Zeitschrift für angewandte Mathematik und Physik ZAMP*, 9(5):748–763, 1958. doi: <https://doi.org/10.1007/BF02424793>.
- [86] M. Zlatić, F. Rocha, L. Stainier, and M. Čanađija. Data-driven methods for computational mechanics: A fair comparison between neural networks based and model-free approaches. *Computer methods in applied mechanics and engineering*, 431:117289, 2024. doi: <https://doi.org/10.1016/j.cma.2024.117289>.